Mon. Not. R. Astron. Soc. **000**, 1–16 (2009) Printed 5 October 2011 (MN LATEX style file v2.2)

Seeking the Imprint of Small-Scale Structure on the Properties of Dark Matter Haloes

C. Power[⋆1,2], J. Bland-Hawthorn[3] & G. F. Lewis[3]
[1] *International Centre for Radio Astronomy Research, University of Western Australia, 35 Stirling Highway, Crawley, Western Australia 6009, Australia*
[2] *Department of Physics and Astronomy, University of Leicester, Leicester, LE1 7RH, United Kingdom*
[3] *Sydney Institute for Astronomy, School of Physics, University of Sydney, New South Wales 2006, Australia*

ABSTRACT

The characteristic prediction of the Cold Dark Matter (CDM) model is that the Universe should contain a wealth of small-scale structure – low-mass dark matter haloes. Yet, because galaxy formation is inefficient in the shallow potential wells of these low-mass haloes, we expect this small-scale structure to be dark. How can we tell the difference between a Universe in which low-mass haloes are present but dark and one in which these systems have never formed? In this paper, we address this question by comparing and contrasting the properties of dark matter haloes in a ΛCDM model and dark matter models in which halo formation is suppressed below a cut-off mass $M_{\rm cut}$, where we choose $5 \times 10^9\,h^{-1}{\rm M}_\odot \lesssim M_{\rm cut} \lesssim 10^{11}\,h^{-1}{\rm M}_\odot$. We investigate the mass function, spatial clustering and mass assembly and merger histories of galaxy- and group-mass haloes, but it is their angular momentum content to which we pay particular attention; we reason that systematic differences in the angular momenta of haloes as a function of $M_{\rm cut}$ could be imprinted on, say, the scale lengths of galaxy discs. However, a battery of measures of halo angular momentum show no clear dependence on $M_{\rm cut}$. These include (i) the spin parameters λ and specific angular momenta j of the halo population as a whole, (ii) the growth of angular momentum of material within the Lagrangian volume that corresponds to individual haloes at z=0, and (iii) the angular momentum distribution of material within individual haloes. We conclude that mergers with low-mass haloes are unimportant in setting a dark matter halo's angular momentum. Based on our results, we discuss the factors that likely determine a halo's spin angular momentum and we consider the prospects for robust astrophysical tests of the nature of dark matter.

Key words: methods: N-body simulations – galaxies: formation – galaxies: haloes – cosmology: theory – dark matter – large-scale structure of Universe

1 INTRODUCTION

One of the key questions facing fundamental physics and cosmology at the turn of the $21^{\rm st}$ century concerns the nature of the dark matter. There is compelling observational evidence to suggest that approximately 80% of the matter content of the Universe is in the form of some exotic, non-baryonic dark matter (cf. Spergel 2007), and the clustering of this dark matter is believed to play a crucial role in the formation and subsequent evolution of galaxies (e.g. White & Rees 1978; White & Frenk 1991). The central assertion of the standard paradigm of cosmological structure formation is that this non-baryonic dark matter is cold – that is, dark matter particles were non-relativistic at the time of decoupling – and this leads to a number of important implications. The most fundamental is that Cold Dark Matter (hereafter CDM) haloes have central density cusps (cf. Tremaine & Gunn 1979; Moore 1994). It is also significant that the CDM halo mass function – the number of haloes of mass M per unit mass per unit comoving volume – predicts an abundance of low-mass haloes whose space density increases with decreasing mass as $M^{-\alpha}$ where $\alpha \sim 2.0$ (e.g. Reed et al. 2007; Lukić et al. 2007), and it may extend down to masses as small as $\sim 10^{-6}{\rm M}_\odot$ (cf. Green et al. 2004).

These two predictions lead to an expectation that the number density of low-mass CDM haloes – small-scale structure – should be large in any finite volume, independent of environment. Indeed, high resolution cosmological N-body simulations of galaxy-mass CDM haloes have shown that the normalised mass function of substructure haloes is indistinguishable from that measured in galaxy cluster mass haloes, and that it continues to increase down to the mass resolution of the simulation (Moore et al. 1999; Klypin et al. 1999; Gao et al. 2004; Diemand et al. 2007). In contrast, analysis of halo formation in dark matter models in which small-scale power

⋆ chris.power@icrar.org

is suppressed at early times shows that the abundance and clustering of substructure is reduced (e.g. Bode et al. 2001; de Vega & Sanchez 2011; Dunstan et al. 2011; Smith & Markovic 2011) whereas mass profiles retain their cuspiness (Colín et al. 2000; Avila-Reese et al. 2001; Knebe et al. 2002; Colín et al. 2008). Therefore it could be argued that it is the abundance of small-scale structure, rather than central density cusps, that is the defining characteristic of the CDM model.

Although the CDM model predicts an abundance of low-mass dark matter haloes, we do not observe a corresponding abundance of low-mass galaxies. This is not surprising because galaxy formation is expected to be inefficient in the shallow potential wells of low-mass haloes (e.g. Dekel & Silk 1986; Efstathiou 1992; Thoul & Weinberg 1996). A galaxy will form once gas collapses onto a halo that is sufficiently massive to support efficient cooling. Cooling is inefficient in haloes with virial temperatures $T_{\rm vir} \lesssim 10^4{\rm K}$ and so we expect haloes less massive than $M \sim 10^9{\rm M}_\odot$ at redshift z=0 to be dark (e.g. Efstathiou 1992). Furthermore, there is now compelling evidence that the Universe underwent a period of reionisation early in its history ($z \gtrsim 6$) during which an ionising background of UV and X-ray radiation was built up that inhibited galaxy formation. The presence of the photo-ionising background at early times prevented the collapse of gas onto low-mass haloes, while radiative cooling and star formation was suppressed in galaxies that formed prior to reionisation (e.g. Benson et al. 2002). For these reasons we would expect that the bulk of small-scale structure in the CDM model will be dark.

The abundance of low-mass haloes may be the defining prediction of the CDM model, but if they remain dark because galaxy formation is inefficient on these mass scales how can we be sure that they are there? What kind of astronomical observation could we make that would allow us to differentiate between the CDM model and a dark matter model in which the formation of low-mass haloes is suppressed? Gravitational lensing by subhaloes would appear a promising tool[1]. It has been possible to construct the high-mass end of the subhalo mass function in galaxy clusters using combined strong and weak lensing measurements of cluster ellipticals (e.g. Natarajan & Springel 2004) that appears to be consistent with the predictions of numerical simulations (Natarajan et al. 2007). Lower mass subhaloes have small lensing cross sections with respect to background sources and so we might expect them to be present as perturbations in the lensing potential of their host. Indeed, it has been speculated that anomalous flux ratios measured in gravitational lenses arise because of such small perturbations (Mao & Schneider 1998; see also Xu et al. 2009), and this has led to an upper limit on the fraction of a host's mass associated with substructure that is consistent with the results of cosmological simulations (e.g. Dalal & Kochanek 2002). However, it has been argued that these anomalous flux ratios can be influenced by structure along the line of sight to the lens (Chen et al. 2003), and that systems in which this effect has been measured can be well fitted by smooth lens models (Evans & Witt 2003).

Galaxy cluster substructure is readily evident as galaxies with (sub)halo masses $M \gg 10^9 h^{-1} M_\odot$. Arguably it is on galaxy scales, where the halo masses of satellites are comparable to $M \sim 10^9 h^{-1} M_\odot$, that the crucial tests are to be made. However, the relatively low number density of background sources make gravitational lensing difficult as a probe of small-scale structure in the halo (but see Lewis et al. 2000). For this reason more indirect probes of small-scale structure are necessary, and the structure of galaxy discs provide an interesting testbed. These are rotationally supported and relatively cold systems, and so it is plausible that encounters between discs and low-mass subhaloes could act as a source of dynamical heating with observable effects. Both Font et al. (2001) and Kazantzidis et al. (2008) have studied encounters between subhaloes and thin galactic discs using subhalo properties (mass function, velocity distribution, orbital eccentricities) drawn from cosmological simulations. Yet it is the encounters between massive subhaloes and the disc that are most damaging, leading to the formation of distinctive features (e.g. rings and bars) and an increase in the scale-height (Kazantzidis et al. 2008); encounters between low-mass subhaloes and the disc have little impact on disc structure (Font et al. 2001).

The presence of low-mass subhaloes may not affect the structure of galaxy discs that are already in place, but could they play a role in setting the structure of the disc as it forms? A galaxy's disc forms when gas accreted by its dark matter halo cools and settles in the halo's potential well, and it has been argued that the angular momenta of the disc and halo should be coupled (e.g. Fall & Efstathiou 1980; Mo et al. 1998; Zavala et al. 2008). In this picture, dark matter and gas are initially well mixed and subject to the same gravitational tidal field, and so they will have similar initial angular momenta. As the gas cools and condenses into a disc, its initial angular momentum is conserved and imprinted on the scale length of the disc (e.g. Fall & Efstathiou 1980; Mo et al. 1998), and it is in this way that halo and disc angular momenta are expected to be connected.

The initial growth of halo angular momentum is driven by tidal torques arising from gravitational interaction with the large scale matter distribution (e.g. White 1984), and so we might not expect differences between CDM and WDM(-like) models. However, once the halo has passed through maximum expansion and the collapse has become non-linear, merging and accretion are believed to play an increasingly important role in determining both the magnitude and direction of the angular momentum (e.g. Bailin & Steinmetz 2005) and it is here that we might anticipate differences between CDM and WDM(-like) models. The analyses of Maller et al. (2002), Vitvitska et al. (2002) and Hetznecker & Burkert (2006), which imply that mergers are crucial drivers of halo angular momentum growth, suggest that there should be differences, whereas recent work by Wang & White (2008), who use Hot Dark Matter simulations to show that universal halo properties (including spin angular momentum) are insensitive to merging history, suggest not.

These considerations prompt us to revisit the role of small-scale structure in the growth of halo angular momentum and to assess its plausibility as a test of the CDM model. We do so using cosmological N-body simulations to examine how the angular momenta and spins of galaxy- and group-mass haloes ($M \sim 10^{11}$ to $10^{13} h^{-1}{\rm M}_\odot$) at late times are affected by the suppressing small-scale power at early times. We compare and contrast haloes forming in a fiducial ΛCDM model with those in models in which we filter the initial power spectrum $P(k)$ such that power is suppressed on spatial scales smaller than $R_{\rm cut} \sim M_{\rm cut}^{1/3}$. Here $M_{\rm cut}$ is the cut-off mass, the mass scale below which halo formation is suppressed, which we vary between $5 \times 10^9 h^{-1}{\rm M}_\odot \lesssim M_{\rm cut} 10^{11} h^{-1}{\rm M}_\odot$. These values of $M_{\rm cut}$ unrealistic in the sense that they are too large to be consistent with observational constraints (see, for example, the recent review of Primack 2009), but they allow us to experi-

[1] We note that gravitational lensing by large-scale structure can be used to place limits on the dark matter particle mass and can rule out particle masses smaller than 1 keV (see, for example, the recent work of Viel et al. 2011; Markovic et al. 2011; Smith & Markovic 2011).

ment with the consequences of progressively more aggressive truncations of the initial power spectrum on the properties of haloes with $M \gtrsim 10^{11}\mathrm{M}_{\odot}$.

By comparing the magnitude and redshift evolution of halo angular momentum and spin in these truncated models with those is a fiducial ΛCDM model, we can assess the importance of small-scale structure in driving angular momentum growth. If there are measurable differences between our fiducial ΛCDM model and the truncated models (which we might expect; cf. Vitvitska et al. 2002; Hetznecker & Burkert 2006) then this offers the possibility that observationally measurable properties of galaxies that are likely coupled to the angular momentum of their haloes – such as the scale lengths of galactic discs (cf. Mo et al. 1998) – could be used to differentiate between dark matter models.

The structure of this paper is as follows. In §2 we describe our simulations, detail how we set up the truncated models and summarise our approach to constructing merger trees. In §3 we begin by focusing on the number density and spatial clustering of the haloes, taking care to demonstrate that the number density and clustering strength of low-mass haloes is suppressed in our truncated models. We show how this suppression in number density and clustering impacts on the number and frequency of minor mergers (§4). Finally we explore in some depth measures of halo angular momentum and spin in the different models and we critically assess the role of small scale structure in the growth of halo angular momentum (§5). In §6 we summarise our results, assessing their implications for understanding the origin of halo spin angular momentum, and we consider the prospects for developing robust astrophysical tests of the nature of the dark matter.

2 THE SIMULATIONS

We have run a sequence of cosmological N-body simulations that follow the formation and evolution of dark matter haloes in a box of side $20h^{-1}\mathrm{Mpc}$ from a starting redshift of z=100 to z=0. For each run we assume a flat cosmology with a dark energy term, and for convenience we adopt the cosmological parameters of Spergel (2007) – matter and dark energy density parameters of $\Omega_{\mathrm{m}} = 0.24$ and $\Omega_{\Lambda} = 0.76$, a dimensionless Hubble parameter of $h = 0.73$, a normalisation of $\sigma_8 = 0.74$ and a primordial spectral index of n_{spec}=0.95. Each simulation volume contains 256^3 equal-mass particles, which for the adopted cosmological parameters gives particle masses of $m_{\mathrm{p}} = 3.176 \times 10^7 h^{-1}\mathrm{M}_{\odot}$.

The respective runs differ in the spatial scale below which small-scale power in the initial conditions is suppressed. We generate a single realisation of the ΛCDM power spectrum appropriate for our choice of cosmological parameters and in the case of the truncated runs we introduce a sharp cut-off in the ΛCDM power spectrum at progressively larger spatial scales. This cut-off spatial scale is set by the mass scale below which we wish to suppress halo formation. Details about the truncated runs are given in the next section.

All of our simulations were run using the parallel TreePM code GADGET2 (Springel 2005) with a constant comoving gravitational softening ϵ=1.5 $h^{-1}\mathrm{kpc}$ and individual and adaptive particle time-steps. These were assigned according to the criterion $\Delta t = \eta\sqrt{\epsilon/a}$, where a is the magnitude of a particle's gravitational acceleration and $\eta = 0.05$ determines the accuracy of the time integration.

Table 1. Truncated Models : Simulation Details

Model	M_{cut} $10^{10}h^{-1}\mathrm{M}_{\odot}$	R_{cut} $h^{-1}\mathrm{Mpc}$	k_{cut} $h\mathrm{Mpc}^{-1}$
A	0.5	0.26	24.01
B	1.0	0.33	19.06
C	5.0	0.56	11.15
D	10.0	0.71	8.85

2.1 Truncated Dark Matter Models

We are interested in models in which small scale power is suppressed at early times. Physically such a suppression arises because the dark matter free streams; this acts as a damping mechanism that washes out primordial density perturbations and introduces a cut-off in the linear matter power spectrum. If the dark matter particle is a thermal relic, the spatial scale at which this cut-off occurs can be calculated (cf. Bergström 2000). This gives a free streaming scale λ_{fs} that can be expressed as

$$\lambda_{\mathrm{fs}} = 0.2\,(\Omega_{\mathrm{dm}}\,h^2)^{1/3}\,\left(\frac{m_{\mathrm{dm}}}{\mathrm{keV}}\right)^{-4/3}\,\mathrm{Mpc}, \qquad (1)$$

where m_{dm} is the dark matter particle mass measured in keV and Ω_{dm} is the dark matter density (cf. Boehm et al. 2005). Provided λ_{fs} is small compared to the spatial scales we are interested in simulating, the power spectrum will differ little from the ΛCDM power spectrum (which itself may have a cut-off on comoving scales of order 1 pc; cf. Green et al. 2004). However, as λ_{fs} increases and approaches the scales that we wish to resolve, then it becomes necessary to determine how the power spectrum changes.

The shape of the linear power spectrum for collisionless WDM models has been calculated by a number of authors (e.g. Bardeen et al. 1986; Bode et al. 2001), and it can be recovered from the CDM power spectrum by introducing an exponential cut-off at small scales. The larger λ_{fs}, the larger the mass scale M_{fs} below which structure formation is suppressed and the smaller the wavenumber k at which the WDM and CDM power spectra differ, although the relationship between λ_{fs} and M_{fs} is sensitive to the precise nature of the WDM particle. However, we do not wish to make any assumptions about the precise nature of the dark matter other than that it is collisionless and that low-mass halo formation is suppressed. Therefore, we follow the approach of Moore et al. (1999) and introduce a sharp cut-off into the power spectrum at k_{cut}, thus suppressing power at wave-numbers $k \geqslant k_{\mathrm{cut}}$. We choose k_{cut} by identifying a mass scale M_{cut} and estimating the comoving length scale R_{cut},

$$R_{\mathrm{cut}} = \left(\frac{3\,M_{\mathrm{cut}}}{4\pi}\,\frac{1}{\overline{\rho}}\right)^{1/3} \qquad (2)$$

where $\overline{\rho}$ is the mean density of the Universe.

Generation of Initial Conditions

We follow the standard procedure of generating a statistical realisation of the high redshift density field using the appropriate linear theory power spectrum, from which initial displacements and velocities are computed and imposed on a suitable uniform particle load; for this study we adopt an initial glass distribution (cf. White 1994). We use the Boltzmann code CMBFAST (Seljak & Zaldarriaga 1996) to generate the CDM transfer function for our choice

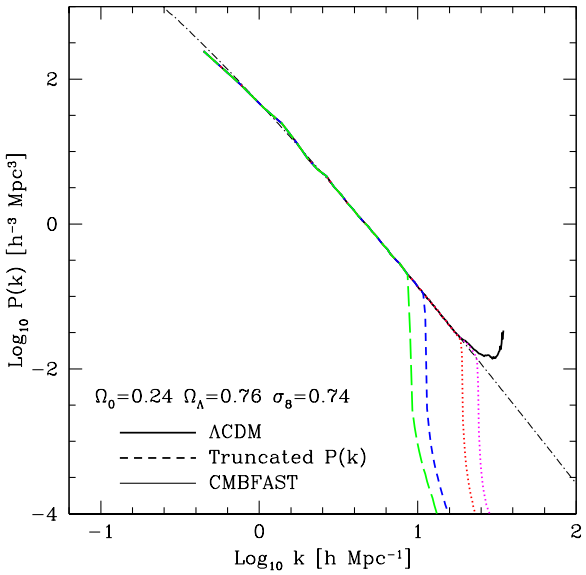

Figure 1. Power Spectra of Initial Conditions at z=0. The heavy solid (dashed) curves represent the power spectra measured from the initial conditions for the 20 h^{-1}Mpc ΛCDM and truncated models respectively, plotted at z=0. The thin solid curve represents the input power spectrum, whose transfer function was computed using CMBFAST.

of cosmological parameters. This is convolved with the primordial power spectrum ($P(k) \propto k$) to obtain the appropriate ΛCDM power spectrum $P(k)$. To obtain a truncated model, we truncate $P(k)$ sharply at $k_{\rm cut} = 2\pi/R_{\rm cut}$ (where $R_{\rm cut}$ is given by equation 2) and thereby suppress power on scales $k \gtrsim k_{\rm cut}$.

We consider five cases – a fiducial ΛCDM model and truncated models in which small scale power is suppressed at masses below $M_{\rm cut} = 5 \times 10^9$, 10^{10}, 5×10^{10} and $10^{11} h^{-1} M_\odot$ respectively. Note that the cut-off wavenumber $k_{\rm cut}$ is always less than the Nyquist frequency of the simulation, $k_{\rm Ny} \simeq 40h\,{\rm Mpc}^{-1}$. Values for the cut-off masses and wave-numbers are given in Table 1. Power spectra measured from the initial conditions of the runs are plotted at z=0 and are shown in figure 1.

2.2 Halo Identification & Merger Trees

Halo Identification: Groups are identified using AHF, otherwise known as **A**MIGA's **H**alo **F**inder (cf. Knollmann & Knebe 2009). AHF locates groups as peaks in an adaptively smoothed density field using a hierarchy of grids and a refinement criterion that is comparable to the force resolution of the simulation (i.e. 5 particles per cell). Local potential minima are calculated for each of these peaks and the set of particles that are gravitationally bound to the peaks are identified as the groups that form our halo catalogue. Each halo in the catalogue is then processed, producing a range of structural and kinematic information.

We adopt the standard definition of a halo such that the virial mass is

$$M_{\rm vir} = 4\pi\rho_{\rm crit}\Delta_{\rm vir} r_{\rm vir}^3/3, \quad (3)$$

where $\rho_{crit} = 3H^2/8\pi G$ is the critical density of the Universe and $r_{\rm vir}$ is the virial radius, which defines the radial extent of the halo. The virial overdensity criterion, $\Delta_{\rm vir}$, is a multiple of the critical density, and corresponds to the mean overdensity at the time of virialisation in the spherical collapse model (the simplest analytic model of halo formation; cf. Eke et al. 1996). In an Einstein-de Sitter Universe, $\Delta_{\rm vir} \simeq 178$, while in the favoured ΛCDM model $\Delta_{\rm vir} \simeq 92$ at z=0.

Defined in this way, the virial radius $r_{\rm vir}$ provides a convenient albeit approximate boundary for a dark matter halo that can be estimated easily from simulation data. However, it is *only* approximate – haloes that form in cosmological simulations are relatively complex structures. They are generally aspherical (e.g. Bailin & Steinmetz 2005) and asymmetric (e.g. Gao & White 2006) with no simple boundary (e.g. Prada et al. 2006), and so defining an appropriate boundary is not straightforward. This presents difficulties when calculating, for example, a halo's angular momentum and its binding energy (cf. Łokas & Mamon 2001). Material bound to the halo can lie outside of $r_{\rm vir}$, and this will distort the angular momentum and binding energy one measures for the *halo* using only material from within $r_{\rm vir}$. This issue has been touched on by previous authors (e.g. Cole & Lacey 1996; Łokas & Mamon 2001; Shaw et al. 2006; Power et al. 2011) in the context of identifying when a halo is in virial equilibrium. In a similar vein, the angular momentum one measures using only material from within $r_{\rm vir}$ will be biased. This is an important caveat that we need to bear in mind when discussing our analysis of halo angular momentum in § 5.

Halo Merger Trees: Halo merger trees are constructed by linking halo particles at consecutive output times;

- For each pair of group catalogues constructed at consecutive output times t_1 and $t_2 > t_1$, the 'ancestors' of 'descendant' groups are identified. For each descendent identified in the catalogue at the later time t_2, we sweep over its associated particles and locate every ancestor at the earlier time t_1 that contains a subset of these particles. A record of all ancestors at t_1 that contain particles associated with the descendent at t_2 is maintained.
- The ancestor at time t_1 that contains in excess of $f_{\rm prog}$ of these particles and also contains the most bound particle of the descendent at t_2 is deemed the main progenitor. Typically $f_{\rm prog} = 0.5$, i.e. the main progenitor contains in excess of half the final mass.

Each group is then treated as a node in a tree structure, which can be traversed either forwards, allowing one to identify a halo at some early time and follow it forward through the merging hierarchy, or backwards, allowing one to identify a halo and all its progenitors at earlier times. In our analysis we concentrate on the main trunk of the merger tree, in which we follow the evolution of the main progenitor of a halo to earlier times.

3 MASS FUNCTIONS & SPATIAL CLUSTERING

As our starting point, we compare and contrast the mass distribution and spatial clustering of dark matter haloes in the ΛCDM and truncated-$P(k)$ models respectively, and we quantify the evolution with redshift of these measures. We expect differences between models to be apparent for haloes with masses $M \sim M_{\rm cut}$ and to become more pronounced with increasing redshift, when $M_{\rm cut}$ is a larger fraction of the typical collapsing mass M^*.

Images: In Figure 2 we show the projected dark matter distribution in thin slices ($20 \times 20 \times 2h^{-3}{\rm Mpc}^3$) taken through the ΛCDM (upper panels), Truncated B (middle panels; hereafter TruncB) and D (lower panels; hereafter TruncD) at z = 0, 1 and 4 (from left to

right). Each slice is centred on the geometric centre of the simulation volume and the grey-scale is weighted by the logarithm of projected density. Figure 2 is instructive because it provides a powerful visual impression of the effect of suppressing small scale power at early times. The filamentary network is relatively unaffected and the positions of the most massive haloes, which form at the nodes of these filaments, are similar in each of the models we have looked at. What is striking, however, is the impact on the abundance of low-mass haloes, which appear as small dense knots in projection. As $M_{\rm cut}$ increases, the projected number density of these low-mass haloes decreases markedly as we go from the ΛCDM run to the TruncD run (top and bottom panels respectively). This is evident in the clustering around more massive haloes and the absence of low-mass systems in the void regions. Furthermore, the contrast between the models becomes increasingly noticeable with increasing redshift – compare z=0 and z=4. This mirrors structure formation in WDM models (see, for example, Figure 4 of Bode et al. 2001).

We note also the presence of the low-mass haloes distributed along filaments in "beads-on-a-string" fashion in the TruncD run, especially at z=0. There is good reason to believe that these haloes are spurious, driven by particle discreteness. The detailed study of Wang & White (2007) has shown that they arise because of unphysical fragmentation of filaments in models in which small-scale power is suppressed. As we show below, the presence of these spurious haloes is apparent in the mass functions we recover from the truncated-$P(k)$ runs and so we must take appropriate care when interpreting our results.

Mass Functions: The maps of projected density reveal that the number density of low-mass haloes decreases in our truncated-$P(k)$ runs, and we examine this quantitatively in Figure 3. In the upper panel, we show the cumulative mass function $N(>M)$ for the different runs at z=0, 1, 2 and 3 (top right to bottom left panels). The cumulative mass function provides a measure of the number density of haloes with masses in excess of M in a comoving volume. For comparison we show the analytic mass function of Sheth & Tormen (1999, 2002) appropriate for our adopted ΛCDM cosmology (thin dotted curves), corrected for the effects of finite volume.[2] In the lower panel we plot the ratios of the mass functions in the truncated-$P(k)$ runs relative to the ΛCDM run.

There is good agreement between the mass functions obtained in the runs for halo virial masses $M_{\rm vir} \gtrsim M_{\rm cut}$ – to better than 10% as can be seen in the plot of $N(>M)/N(>M)_{\rm CDM}$ against $M_{\rm vir}$. This can be understood by considering the mass variance of the linear density field $\sigma(M)$, which regulates when a particular mass scale collapses and virialises; $\sigma(M)$ is not particularly sensitive to the form of the power spectrum on small scales, and so it should be insensitive to suppression of small scale power at early times.

Differences between the ΛCDM and truncated-$P(k)$ runs become apparent for $M_{\rm vir} \lesssim M_{\rm cut}$, and are most easily observed in the divergence of the respective $N(>M)/N(>M)_{\rm CDM}$ curves from unity. We note that the mass M at which $N(>M)/N(>M)_{\rm CDM}$ begins to deviate significantly – that is, by more than 10% – from unity is approximately a factor of 2 to 2.5 smaller than $M_{\rm cut}$.

[2] Previous studies (e.g. Bagla & Ray 2005; Power & Knebe 2006) have shown that the absence of long wavelength perturbations in boxes of length $\lesssim 100\,h^{-1}$Mpc will lead to a depletion of higher mass haloes and an enhancement of intermediate mass haloes, relative to theoretical expectation. It is possible to correct for such finite volume effects and we follow Lukić et al. (2007) by subtracting the mass variance on the scale of the box.

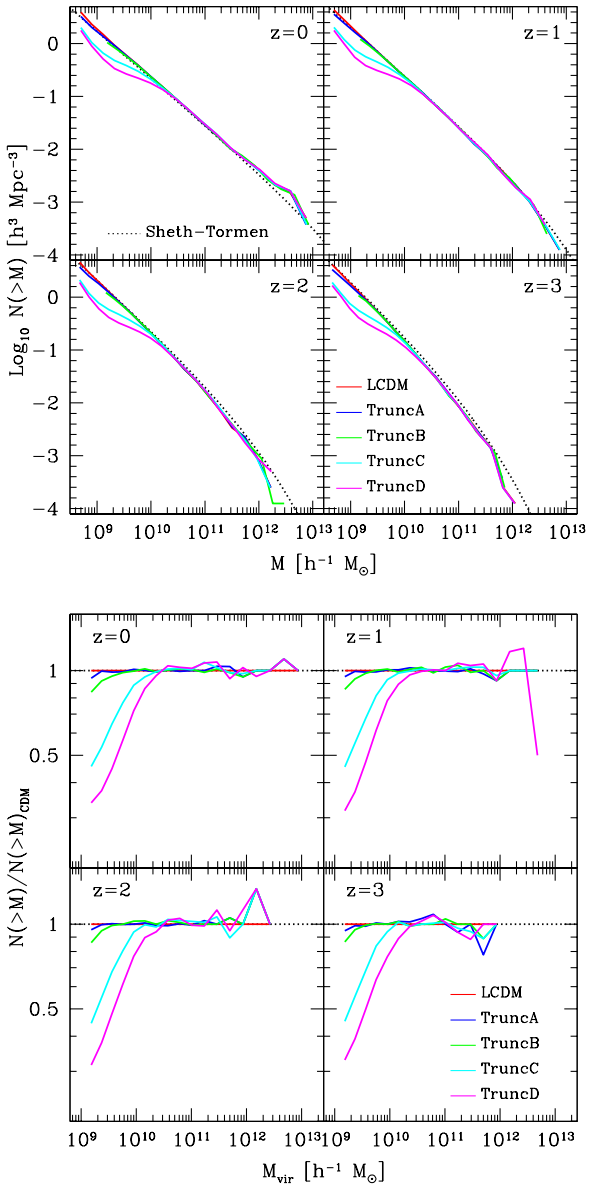

Figure 3. Evolution of the Halo Mass Function with Redshift. (*Upper Panel*) The heavy solid curves in each panel show the mass function measured from the simulations at z=0, 1, 2 and 3 – the fiducial ΛCDM run (red), TruncA with $M_{\rm cut} = 5 \times 10^9 h^{-1} M_\odot$ (blue), TruncB with $M_{\rm cut} = 10^{10} h^{-1} M_\odot$ (green), TruncC with $M_{\rm cut} = 5 \times 10^{10} h^{-1} M_\odot$ (cyan), and TruncD with $M_{\rm cut} = 10^{11} h^{-1} M_\odot$ (magenta). The thin dashed curves correspond to the predicted mass function of Sheth & Tormen (1999), computed using the input initial power spectra for the respective simulations. (*Lower Panel*) The heavy solid curves show the ratio of the mass functions measured in runs TruncA to TruncD with respect to the mass function measured in the fiducial ΛCDM run.

We note also that the presence of the spurious haloes that we identified as "beads-on-a-string" in Figure 2 is evident in the cumulative mass function. Rather than flattening off with decreasing mass as predicted by, say, the analytic expression of Sheth & Tormen (1999) for our choice of power spectrum, the mass function increases sharply below a particular mass scale that increases with increasing $M_{\rm cut}$. This effect has been explored by Wang & White (2007) for Hot Dark Matter simulations, and they find that this

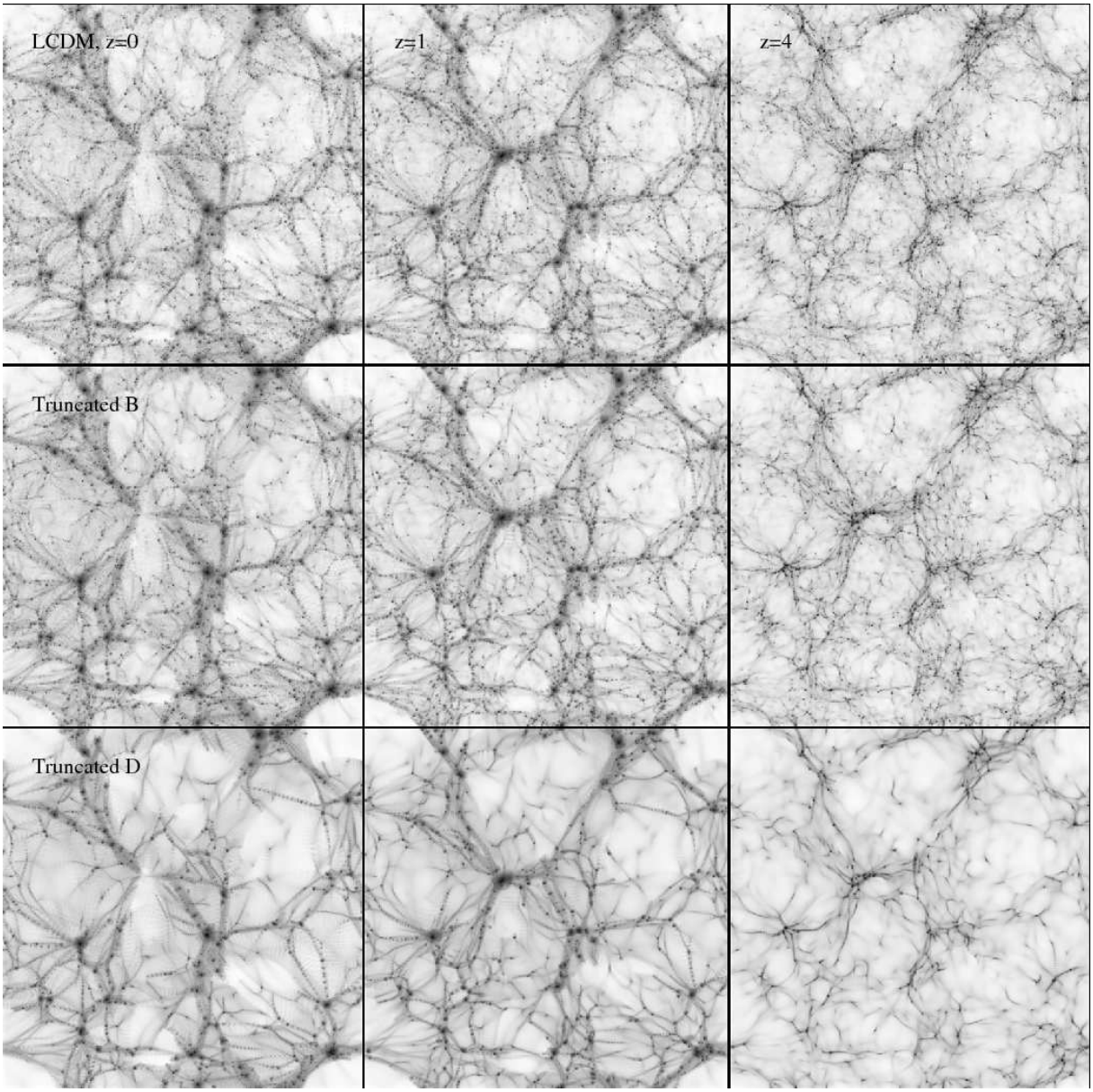

Figure 2. The projected density distribution in $2h^{-1}\mathrm{Mpc}$ slices taken through the centres of each of the boxes. We have smoothed the particle mass using an adaptive Gaussian kernel and projected onto a mesh. Each mesh point is weighted according to the logarithm of its projected surface density, and so the "darker" the mesh point, the higher the projected surface density.

"limiting" mass $\mathrm{M_{lim}}$ can be expressed as $\mathrm{M_{lim}} \simeq 10.1 \overline{\rho}\, d\, k_{\mathrm{peak}}^{-2}$, which we rewrite as,

$$\mathrm{M_{lim}} \simeq 26.2 \left(\frac{m_p}{10^{10}h^{-1}M_{\odot}}\right)^{1/3} \left(\frac{M_{\mathrm{cut}}}{10^{10}h^{-1}M_{\odot}}\right)^{2/3} h^{-1}M_{\odot} \quad (4)$$

where m_p is the particle mass. Careful inspection of their Figure 9 suggests that this corresponds to the minimum mass below which the mass function deviates by more than 10% from the $M^{-0.2}$ power-law. Using equation 4, we compute $\mathrm{M_{lim}} \simeq (2.42, 3.85, 11.26, 17.89) \times 10^{10}h^{-1}\mathrm{Mpc}$ for the runs TruncA, TruncB, TruncC and TruncD respectively. These numbers are systematically larger than the ones we infer from Figure 3, by factors of $\sim (7.7, 5.6, 3.6)$ for the TruncB to TruncD runs[3]. This suggests that the Wang & White (2007) criterion is probably overly conservative when applied to WDM-like models, although a more detailed exploration of convergence issues in such cosmologies would appear necessary.

Spatial Clustering: In Figure 4 we investigate how the clustering strength of haloes differs between the different dark matter models and as a function of redshift. Typically clustering strength is quantified by the correlation function $\xi(r)$, which measures the excess

[3] We note that the TruncA run never deviates by more than 10% from the ΛCDM case.

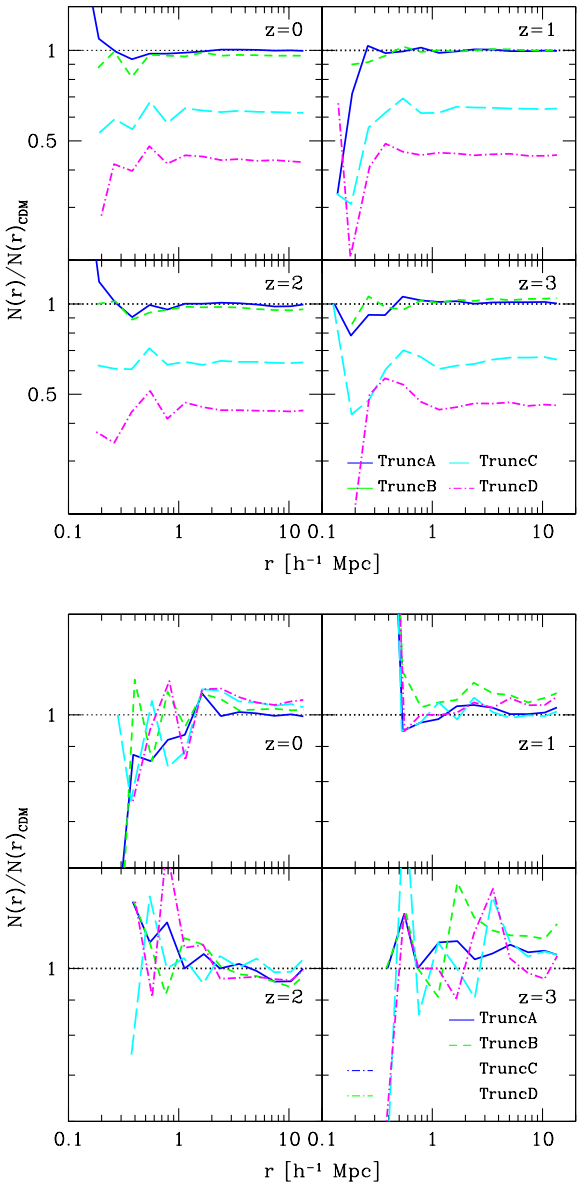

Figure 4. Evolution of Spatial Clustering with Redshift. We examine how the 2-point clustering of pairs of haloes with virial masses in excess of $M_{\rm vir} \geqslant 10^9 h^{-1} M_\odot$ (upper panel) and $10^{11} h^{-1} M_\odot$ (lower panel) varies with redshift.

probability over random that a pair of haloes i and j will be separated by a distance $r = |\vec{r}| = |\vec{r}_i - \vec{r}_j|$. $\xi(r)$ is estimated using

$$\xi(r) = 1 + \frac{\overline{DD(r)}}{\overline{RR(r)}}, \qquad (5)$$

where $\overline{DD(r)}$ is the number of objects (haloes) at a separation r compared to the number in a random distribution $\overline{RR(r)}$. Because we wish to identify differences between the truncated-$P(k)$ and ΛCDM runs, we look at the ratio of $N(r) = \overline{DD(r)} = \overline{RR(r)}(1+\xi(r))$ to $N(r)_{\rm CDM}$. In Figure 4, we show how $N(r)/N(r)_{\rm CDM}$ varies with radius for haloes in the TruncA (solid curves), TruncB (short dashed curves), TruncC (long dashed curves) and TruncD (dotted-dashed curves) at z=0, 1, 2 and 3. We consider halo pairs where the primary mass is $M_{\rm vir} \geqslant 10^{11} h^{-1} {\rm M}_\odot$ and the secondary mass is $M_{\rm vir} \geqslant 3 \times 10^9 h^{-1} {\rm M}_\odot$ in the left hand panels, and primaries and secondaries where $M_{\rm vir} \geqslant 10^{11} h^{-1} {\rm M}_\odot$ in the right hand panels.

This reveals that the clustering strength of low-mass haloes around high mass haloes (i.e. $M_{\rm vir} \geqslant 10^{11} h^{-1} {\rm M}_\odot$) decreases with increasing $M_{\rm cut}$, although the dependence on $M_{\rm cut}$ does not appear to be straightforward. In the TruncA and TruncB runs, we find that $N(r)/N(r)_{\rm CDM}$ is close to unity out to $r \simeq 10 h^{-1}$ Mpc, never deviating by more than 10% to within $\sim 500 h^{-1}$kpc at all redshifts. For the TruncC and TruncD runs, the suppression in clustering strength is quite marked – by $\sim 40\%$ for the TruncC run and $\sim 50\%$ for the TruncD run. Large deviations at small radii reflect the small numbers of very close pairs. In contrast, the clustering strength of massive haloes (i.e. $M \geqslant 10^{11} h^{-1} {\rm M}_\odot$) does not appear to be affected by $M_{\rm cut}$, as we inferred from Figure 2. The ratio $N(r)/N(r)_{\rm CDM}$ is noisy – reflecting the lower number density of massive haloes – but it is approximately unity between $0 \lesssim z \lesssim 3$.

4 MASS ACCRETION & MERGING HISTORIES

The results so far confirm that suppressing small scale power at early times leads to a reduction in the number density of low-mass haloes and their clustering around massive haloes ($M_{\rm vir} \gtrsim 10^{11} h^{-1} {\rm M}_\odot$) at $z \lesssim 3$. This implies that the number of neighbouring low-mass haloes and therefore the number of likely minor mergers a typical halo will experience during a given period should decline with increasing $M_{\rm cut}$. We expect this to depend on both halo mass and epoch. At a given z, the merging history of haloes with masses $M_{\rm vir} \sim M_{\rm cut}$ should be more sensitive to the abundance of small scale structure than haloes with masses $M_{\rm vir} \gg M_{\rm cut}$. Similarly, at earlier times when the typical collapsing mass M^* is smaller and $M_{\rm cut}$ is a larger fraction of M^*, we would expect the effect of suppressing small scale structure to be more pronounced.

When computing mass accretion and merging rates, we use merger trees for all haloes between $5 \times 10^{10} h^{-1} {\rm M}_\odot$ (~ 1600 particles) and $10^{13} h^{-1} {\rm M}_\odot$ at z=0. Note that we have a hard lower limit of 100 particles for a halo to be retained in our catalogues; this corresponds to a mass of $\sim 3.2 \times 10^9 h^{-1} {\rm M}_\odot$, and so we cannot identify minor mergers with mass ratios of less than $\sim 6\%$ in our most poorly resolved haloes.

Formation Redshift: Following the convention of Cole & Lacey (1996), we define the formation redshift $z_{\rm form}$ of a halo identified at z as the redshift $z_{\rm form} > z$ at which the virial mass of the halo's main progenitor first exceeds half of its virial mass at z. This can be estimated from a halo's merger tree by tracking the redshift evolution of its most massive progenitor. We expect $z_{\rm form}$ to correlate with virial mass in any hierarchical model, of which the ΛCDM model is a prime example – on average, more massive systems tend to form later than less massive systems. However, in models in which small scale power is suppressed at early times, we expect this correlation to break down; above $M_{\rm cut}$ we expect halo formation to proceed in a hierarchical manner, from the "bottom-up", whereas below $M_{\rm cut}$ we expect haloes to form via fragmentation, from the "top-down", and so the correlation should invert (i.e. lower mass systems will form progressively later).

In Figure 5, we show the distribution of $z_{\rm form}$ against halo virial mass $M_{\rm vir}$ for haloes identified at z=0. Crosses correspond to $z_{\rm form}$ estimated for individual haloes, while heavy filled squares correspond to the median $z_{\rm form}$ (based on logarithmic bins of

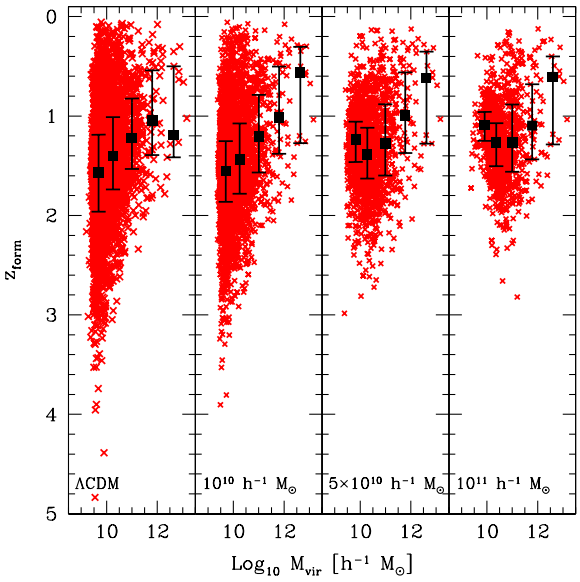

Figure 5. Impact on Halo Formation Time. For each halo at z=0, we follow the main branch of its merger tree to higher redshifts and determine the redshift at which the virial mass of the halo's most massive progenitor first exceeds half the virial mass at z=0. We define this redshift as the formation time of the halo. In this figure we show how the formation time correlates with the virial mass of the halo at z=0. Heavy black squares correspond to median value within each mass bin (0.5 dex wide); error bars show the $10^{\rm th}$ and $90^{\rm th}$ percentiles of the distribution of formation times at that mass.

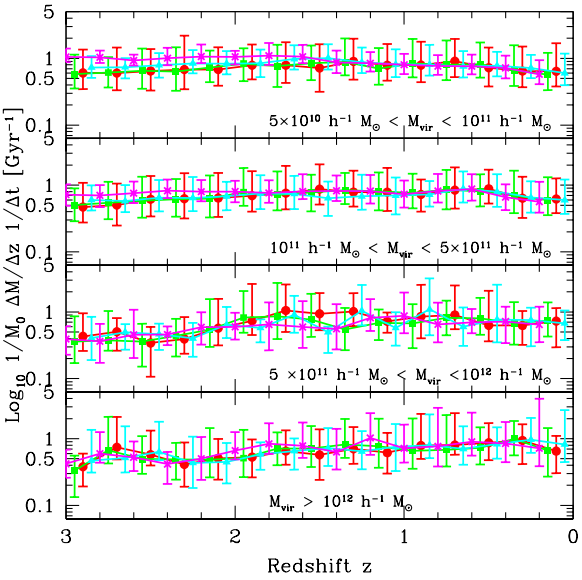

Figure 6. Impact on Mass Accretion Rate. For each halo at z=0, we follow the main branch of its merger tree to higher redshifts and compute the difference in virial mass between progenitors at z_0 and $z_1 > z_0$. From this we compute the mass accretion rate with respect to time (in Gyrs), normalised by the virial mass of the descendent halo at z=0. Within each of the mass bins we compute the average mass accretion rate for haloes in the fiducial ΛCDM run (red filled circles), TruncB ($M_{\rm cut} = 10^{10}h^{-1}M_{\odot}$; green filled squares),TruncC ($M_{\rm cut} = 5 \times 10^{10}h^{-1}M_{\odot}$; cyan filled triangles) and TruncD ($M_{\rm cut} = 10^{11}h^{-1}M_{\odot}$; magenta crosses).

0.5 dex in mass). The expected trend is readily apparent in the ΛCDM run and in the truncated-$P(k)$ runs for haloes with masses in excess of $M_{\rm cut}$. Indeed, we find that the median formation times of haloes with masses above $M_{\rm cut}$ in the truncated-$P(k)$ are in close agreement with those in the ΛCDM run – the absence of small-scale structure has little bearing on when massive haloes form. For haloes with masses below $M_{\rm cut}$ we note that the relation between $z_{\rm form}$ and $M_{\rm vir}$ flattens off and in the two runs with the most extreme values of $M_{\rm cut}$ (TruncC with $M_{\rm cut} = 5 \times 10^{10}h^{-1}{\rm M}_{\odot}$ and TruncD with $M_{\rm cut} = 10^{11}h^{-1}{\rm M}_{\odot}$) the relation inverts so that as $M_{\rm vir}$ decreases, $z_{\rm form}$ decreases. While we might expect such an inversion to occur, it is not straightforward to determine how the spurious haloes that we noted in the previous section affect this result.

Mass Accretion Rate: The formation redshift provides an integral measure of the rate at which a halo's mass has been assembled; haloes with low $z_{\rm form}$ have assembled more recently and therefore have higher mass accretion rates at z=0. In Figure 6 we show how the mass accretion rate of the most massive progenitors of haloes identified at z=0 evolves with redshift. This accretion rate includes both smooth accretion and minor and major mergers, although we note that the distinction between minor mergers and smooth accretion is a moot one, especially in a CDM model; as the mass and force resolution of the simulation increases, we can in principle resolve increasing numbers of low-mass haloes.

From upper to lower panels, we show the average accretion rate as a function of redshift for haloes with virial masses at z=0 in the range $5 \times 10^{10} \leqslant M_{\rm vir}/h^{-1}{\rm M}_{\odot} \leqslant 10^{11}$ (filled circles), $10^{11} \leqslant {\rm M_{vir}}/{\rm h}^{-1}{\rm M}_{\odot} \leqslant 5 \times 10^{11}$ (filled squares), $5 \times 10^{11} \leqslant M_{\rm vir}/h^{-1}{\rm M}_{\odot} \leqslant 10^{12}$ (filled triangles) and $M_{\rm vir}/h^{-1}{\rm M}_{\odot} \leqslant 10^{12}$ (crosses). Note that we measure the accretion rate as the change in virial mass (ΔM) per unit redshift (Δz) per unit time (Δt), normalised by the final (i.e. z=0) virial mass. Error bars indicate r.m.s. scatter.

Figure 6 shows that haloes accrete their mass at similar rates across the different models, regardless of whether or not small scale power is suppressed at early times. On average, less massive haloes tend to have higher accretion rates at $z \gtrsim 1$ than their more massive counterparts, but this rate starts to drop $z \sim 1$ and declines steadily to z=0. In contrast, more massive haloes accrete their mass at a steady rate. We find that our accretion rates for ΛCDM haloes are in good agreement with those reported by Maulbetsch et al. (2007).

Merger Rates: In Figure 7, we focus on the merger rate $\Delta N/\Delta z/\Delta t$ and its variation with redshift. Here differences between runs are immediately apparent and in the sense that we expect – as $M_{\rm cut}$ increases, the merging rate decreases. Note that the estimated merger rate is quite noisy in the lowest mass bin (upper panel), especially at early times – in this case, the lower limit of 100 particles imposed by our halo catalogues corresponds to a merger of progressively greater mass ratio with increasing redshift. For this reason, we focus on haloes with masses at z=0 in excess of $10^{11}h^{-1}M_{\odot}$. For haloes with masses between $10^{11} \leqslant M_{\rm vir}/h^{-1}{\rm M}_{\odot} \leqslant 5 \times 10^{11}$, we find that the average merger rate in the TruncC (TruncD) model is a factor of $\sim 3(1.5)$ smaller than that in the fiducial ΛCDM model, and this is approximately constant with redshift. The difference is less pronounced for haloes with masses between $5 \times 10^{11} \leqslant M_{\rm vir}/h^{-1}{\rm M}_{\odot} \leqslant 10^{12}$, and for

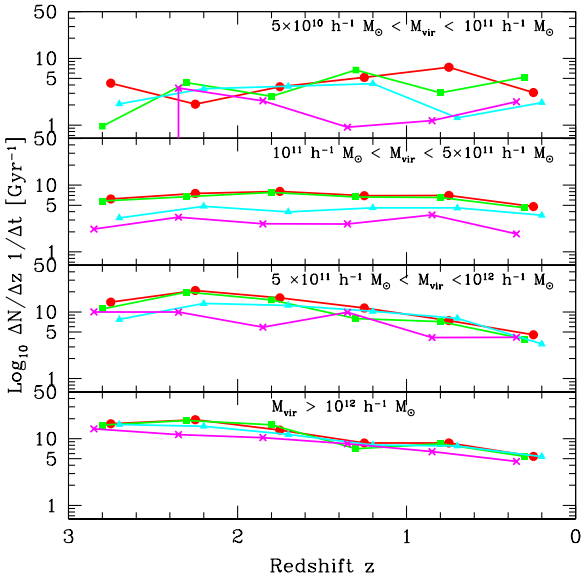

Figure 7. Impact on Merger Rate. For each halo at z=0, we follow the main branch of its merger tree to higher redshifts and determine the number of mergers with mass ratios in excess of 6% experienced by the halo between z_0 and $z_1 > z_0$. From this we compute the merger rate per unit redshift per unit time. Within each of the mass bins we compute the average merger rate for haloes in the fiducial ΛCDM run (red filled circles), TruncB ($M_{\rm cut} = 10^{10}h^{-1}{\rm M}_\odot$; green filled squares), TruncC ($M_{\rm cut} = 5\times10^{10}h^{-1}{\rm M}_\odot$; cyan filled triangles) and TruncD ($M_{\rm cut} = 10^{11}h^{-1}{\rm M}_\odot$; magenta crosses).

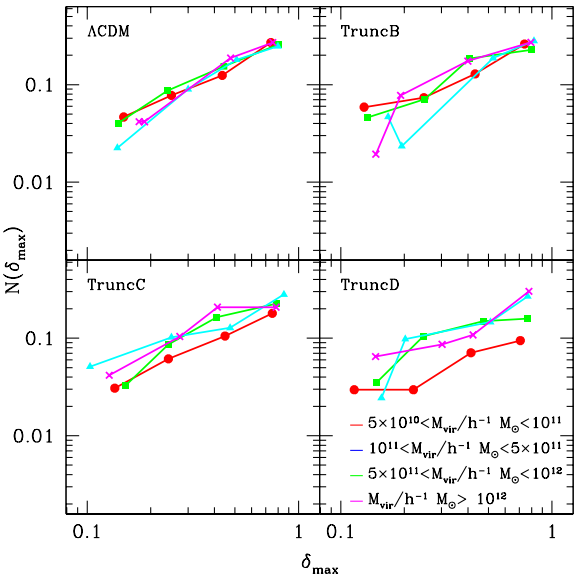

Figure 8. Distribution of Most Significant Mergers. For each halo at z=0, we compute the mass ratio of the most significant merger $\delta_{\rm max}$ that it has experienced since z=0.6 and construct the frequency distribution of $\delta_{\rm max}$ for the respective models.

haloes with masses in excess of $10^{12}h^{-1}{\rm M}_\odot$ there is no discernible difference in the merging rates with redshift.

How are major mergers affected by suppression of small scale power at early times? Figure 8 demonstrates that the likelihood that the mass ratio of the most significant merger experienced by a halo since $z \simeq 0.5$ does not depend strongly on whether or not small scale structure has been suppressed. Here we follow Power et al. (2011) and compute the distribution of the most significant merger $\delta_{\rm max} = M_{\rm acc}/M_{\rm vir}$ experienced by each halo (identified at z=0) between $0 \leqslant z \lesssim 0.5$, split according to virial mass at z=0. The redshift interval $0 \leqslant z \lesssim 0.6$ corresponds to ∼2 dynamical times. There are a number of interesting trends in this Figure. The first is that most significant mergers with large mass ratios (i.e. minor mergers) are relatively uncommon; the probability distribution increases approximately as a power law with $\delta_{\rm max}$ as $\delta_{\rm max}^{1.2}$. The second is that, in the CDM model, the likelihood that a halo experiences a most significant merger with a given $\delta_{\rm max}$ does not depend strongly on its mass. For example, a halo with virial mass of $10^{11}h^{-1}{\rm M}_\odot$ is as likely to have experienced a major merger with mass ratio of ∼ 50% as a $10^{13}h^{-1}M_\odot$ halo – approximately 20%. The third is that there is some evidence that haloes in the mass range $5\times10^{10} \leqslant M_{\rm vir}/h^{-1}{\rm M}_\odot \leqslant 10^{11}$ are less likely to experience major mergers with mass ratios in excess of ∼ 50% (compare TruncB and TruncD).

5 ANGULAR MOMENTUM CONTENT

We have shown that suppressing small scale power at early times affects the abundance and the clustering strength of low-mass haloes at later times. Furthermore, we have demonstrated that by reducing the abundance of low-mass haloes in this way, the number and frequency of minor mergers is also reduced. There is some evidence that the number of major mergers at masses $M_{\rm vir} \sim M_{\rm cut}$ may be affected, although this statement depends on both mass and epoch – at higher redshifts when the typical collapsing mass M^* is lower, the likelihood of a major merger will decline as M^* approaches $M_{\rm cut}$. Do we see systematic differences in the angular momentum content of haloes in the different models we have looked at?

Spin Parameter: We begin our analysis of halo angular momentum by considering the spin parameter λ. A halo's spin parameter is closely related to its angular momentum, quantifying the degree to which the halo is supported by rotation. There are a number of definitions for spin in common usage (e.g. Bullock et al. 2001), but we focus on the "classical" spin parameter of Peebles (1969),

$$\lambda = \frac{J|E|^{1/2}}{GM_{\rm vir}^{5/2}}. \qquad (6)$$

Here J and E are the total angular momentum and binding energy respecively of material with $r_{\rm vir}$ and G is the gravitational constant. We impose a lower limit of 600 particles within $r_{\rm vir}$ ($M_{\rm vir} \geqslant 2\times10^{10}h^{-1}\,{\rm M}_\odot$) when measuring λ; this ensures that both J and E are unaffected by discreteness effects (cf. Power et al. 2011).

In Figure 9 we show how the median spin of the halo population evolves with redshift. In the upper panel we focus on the haloes with $M_{\rm vir} \geqslant 2\times10^{10}h^{-1}M_\odot$, while in the lower panel we consider haloes with $M_{\rm vir} \geqslant 10^{11}h^{-1}M_\odot$. Filled circles, squares, triangles and crosses represent the median spin of the halo populations in the ΛCDM , TruncB, TruncC and TruncD runs, and error bars indicate the 25$^{\rm th}$ and 75$^{\rm th}$ percentiles of the distribution. This figure suggests that the behaviour of the distribution of λ is sensitive to $M_{\rm cut}$ – systematic differences are apparent in the TruncC and TruncD runs when we include all haloes with $M_{\rm vir} \geqslant 2\times10^{10}h^{-1}M_\odot$, whereas the distributions are statistically

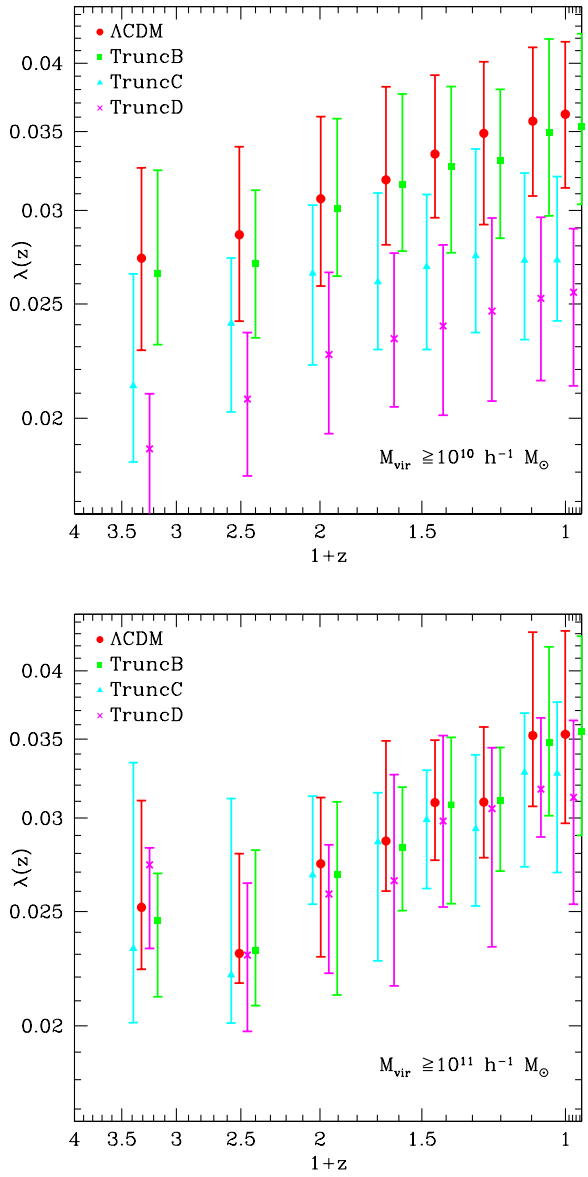

Figure 9. Variation of Median λ with Redshift. We show how the median spin parameter $\lambda_{\rm med}$ varies with expansion factor. In the left hand panel we consider all haloes with virial masses in excess of $M_{\rm vir} \geqslant 1.9 \times 10^{10} h^{-1} M_{\odot}$, while in the right hand panel we consider all haloes that satisfy $M_{\rm vir} \geqslant 10^{11} h^{-1} M_{\odot}$. Lower and upper error bars represent the $45^{\rm th}$ and $55^{\rm th}$ percentiles. The filled circles, squares, triangles and crossed correspond to the fiducial ΛCDM, TruncB, TruncC and TruncD runs respectively.

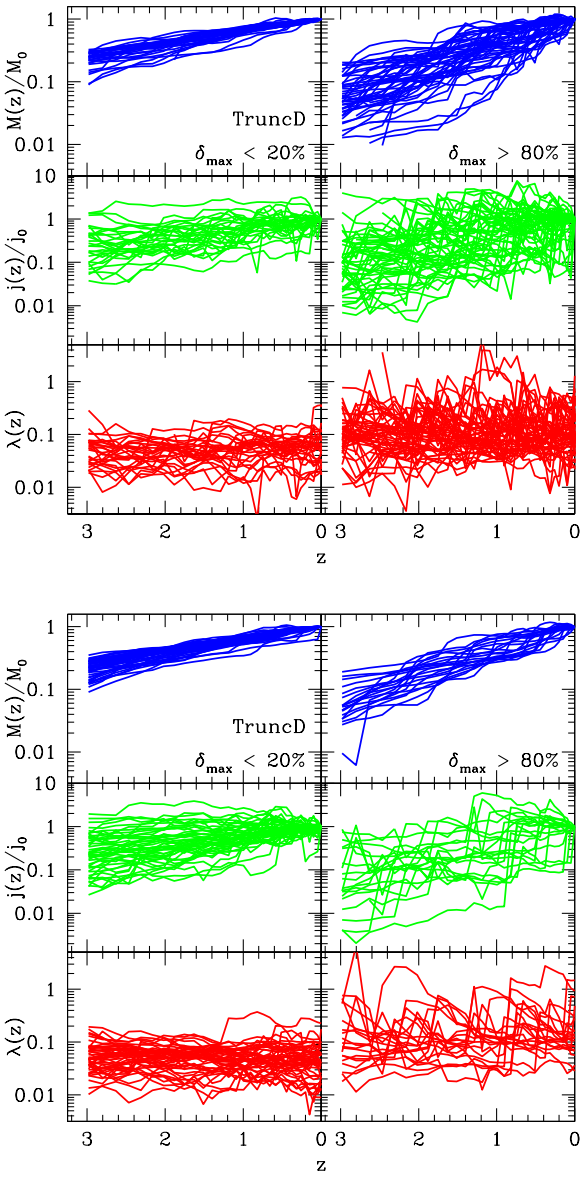

Figure 10. Variation of λ and j with Redshift for Relaxed and Unrelaxed Haloes. We use the merging histories of haloes to identify two samples of haloes, one with a quiescent merging history ($\delta_{\rm max} \lesssim 0.2$ since z=3.0; left hand panels) and one with a violent merging history ($\delta_{\rm max} \gtrsim 0.8$ over the same period; right hand panels) in the ΛCDM and TruncD runs (upper and lower panels respectively). Haloes are chosen such that their virial mass at z=0 satisfies $M_{\rm vir} \geqslant 10^{11} h^{-1} M_{\odot}$ (~ 3000 particles). The upper, middle and lower panels show the growth of halo virial mass (normalised to the virial mass at z=0), concentration $C_{1/5} = r_{\rm vir}/r(M < 0.2\,M_{\rm vir})$ and dimensionless spin parameter $\lambda = J|E|^{1/2}/GM_{\rm vir}^{5/2}$ as a function of expansion factor a. Further details are presented in Table 3.

similar when we include only haloes with $M_{\rm vir} \geqslant 10^{11} h^{-1} M_{\odot}$. This is illustrated in table 2, which summarises how the distribution of spins changes with redshift; here we determine the best-fitting parameters to the functional form proposed by Bett et al. (2007),

$$P(\log \lambda) = A(\lambda/\lambda_0)^3 \exp(-\alpha(\lambda/\lambda_0)^{3/\alpha}); \qquad (7)$$

here A, λ_0 and α are fitting parameters.

This figure is interesting because we include a large population of haloes in the TruncC and TruncD runs with $M_{\rm vir} \leqslant M_{\rm cut}$ when we include haloes with $M_{\rm vir} \geqslant 2 \times 10^{10} h^{-1} M_{\odot}$, and so the apparent differences are to be expected. In contrast, we do not see any evident differences when we include haloes with $M_{\rm vir} \geqslant 10^{11} h^{-1} M_{\odot}$. This is also interesting because it reveals that the median λ increases with decreasing redshift at approximately the same rate – in proportion to $(1+z)^{-0.3}$ – regardless of whether or not we include haloes with masses below $M_{\rm cut}$.

In Figure 10 we focus on individual haloes, showing how λ and the specific angular momentum $j = J/M$ vary with redshift

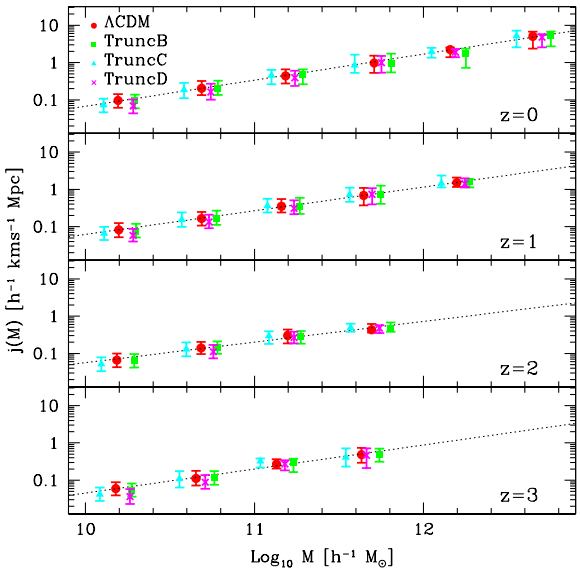

Figure 11. Variation of Specific Angular Momentum $j(M)$ with Virial Mass. Filled circles, squares, triangles and crossed correspond to the fiducial ΛCDM, TruncB, TruncC and TruncD runs respectively.

z for a selection of haloes with quiescent and violent merging histories, drawn from haloes with $M_{\rm vir} \geqslant 10^{11}h^{-1}{\rm M}_{\odot}$ over the redshift interval $0 \leqslant z \leqslant 3$. For each halo we determine the most significant merger $\delta_{\rm max}$ that it has experienced since z=1, where we define $\delta_{\rm max}$ as the mass ratio of the most major merger experienced by the main progenitor of a halo identified at z=0 during the redshift interval $0 \leqslant z \leqslant 1$ (cf. Power et al. 2011). This gives a distribution of $\delta_{\rm max}$ and we identify haloes in the upper (lower) 20% of the distribution as systems with violent (quiescent) merging histories. For ease of comparison, we focus on the extremes – the ΛCDM and TruncD runs (top and bottom respectively).

It is evident from the mass accretion histories shown in the upper panels that $\delta_{\rm max}$ is a useful indicator of how active a halo's merging history is. None of the haloes in our quiescent sample have grown by more than a factor of ~ 10 in mass since z=3; contrast with haloes in the violent sample, some of which have grown by as much as a factor of ~ 100. Interestingly we observe a number of outliers in the violent sample in the ΛCDM run that have no clear analogues in the TruncD run, although this does not significantly affect the median mass accretion rate.

There are two points worthy of note in relation to the evolution of the spin parameter with redshift; the first is that the spin parameter for a given halo is a very noisy quantity but if we consider the average behaviour of haloes in the respective samples, we do not find any clear correlation between spin and redshift (see values for the logarithmic slope γ and Spearman rank coefficient $r_{\rm s}$ in Table 3). The second is that there is a clear offset between median spins in the quiescent and violent samples – haloes with violent merging histories tend to have higher spins (by factors of $\sim$ 3-4) than haloes with quiescent histories. However, there is appreciable scatter over any given halo's history – the r.m.s. variation is ~ 0.25-0.29 for haloes in the quiescent sample and ~ 0.39-0.42 in the violent sample.

The specific angular momentum j for a given halo increases with cosmic time, which we would expect given that the halo is growing and specific angular momentum correlates strongly with mass (see Figure 11). It would appear that the rate of growth of j/j_0 is higher for haloes with violent mass accretion histories – as $j \propto (1+z)^2$ compared to $j \propto (1+z)$ for haloes in the quiescent sample – but as for λ, there is appreciable scatter in j (an r.m.s. variation of ~ 0.3 for the quiescent sample, ~ 0.5 for the violent sample).

These results – tracking the growth of spin and specific angular momentum over the lifetimes of individual haloes – are interesting for a number of reasons. They confirm that, above the mass cut-off $M_{\rm cut}$, there are no statistically significant differences between haloes that form in the ΛCDM and truncated-$P(k)$ runs. Arguably of more importance is the observation that the average spin for haloes that are identified as having quiescent or violent mass accretion histories does not appear to depend on redshift. An individual halo's spin history tends to be quite noisy, but when averaged the spin evolution is at best a weak function of redshift. Finally, we note that that the outliers present in the mass accretion histories of the violent sample in the ΛCDM run but absent in the TruncD are suggestive. It would appear that 3 systems ($\sim 5\%$ of the sample) with $M_{\rm vir} \geqslant 10^{11}h^{-1}M_{\odot}$ in the ΛCDM run have increased their mass a factor of ~ 50 since $z \simeq 1.5$. Inspection of similar figures for the TruncA, TruncB and TruncC runs indicate that the presence or absence of such outliers is dependent on the value of $M_{\rm cut}$ – as $M_{\rm cut}$ increases, the likelihood of such outliers decreases.

Angular Momentum of the Lagrangian Volume: So far we have considered how the spin and angular momentum evolves with cosmic time for haloes that are themselves growing in mass with cosmic time. In Figure 12 we investigate the angular momentum of the Lagrangian region corresponding to the virialised halo at z=0 and determine how it evolves with time for haloes with masses in excess of $5 \times 10^{10}h^{-1}{\rm M}_{\odot}$ at z=0. In other words, we track the angular momentum of all the material that contributes to the final halo at z=0. We identify particles at z=9 that reside within the virial radius at z=0 and compute their angular momentum $\vec{J}$ using their centre of mass and centre of mass velocity. In addition we estimate the mean radial velocity of this material with respect to the centre of mass velocity and determine the redshift at which it changes sign from positive to negative (i.e. from expansion to contraction); this defines the redshift of turnaround z_t. This is typically between $0.6 \lesssim z \lesssim 4$ for the haloes we consider. This is equivalent to one of the two empirical measures of turnaround employed by Sugerman et al. (2000).

We expect tidal torques arising from gravitational interaction with the surrounding matter distribution to drive the growth of angular momentum at early times (prior to turnaround) and so it should not be particularly sensitive to a small scale cut-off in the power spectrum. Linear perturbation theory should hold, and the angular momentum of the material should grow in proportion to $(1+z)^{-3/2}$ (cf. White 1984). Therefore, we expect the angular momentum at turnaround to be close to its maximum value[4] and the frequency distribution of angular momenta should be similar in each of the models we have looked at. Linear perturbation theory no longer provides a good description of angular momentum growth subsequent to turnaround and non-linear processes (i.e. mergers)

[4] Sugerman et al. (2000) have shown that the angular momentum continues to grow 'quasi-linearly' after turnaround until first shell crossing, at which point it reaches its maximum value.

Table 2. Evolution of Spin Distribution with Redshift. N give the number of haloes with masses in excess of $10^{10}, 10^{11}h^{-1}\mathrm{M}_{\odot}$; $\lambda_{\rm med}$ are the median spin values from the measured distributions; and A and λ_0 are best-fits to 7.

Run	N_{11}	$\lambda^{11}_{\rm med}$	A_{11}	λ^{11}_0	N_{10}	$\lambda^{10}_{\rm med}$	A_{10}	λ^{10}_0
z=0								
ΛCDM	220	0.037704	3.0	0.041	1681	0.036696	2.66	0.041
TruncB	215	0.032251	3.0	0.036	1671	0.036483	3.0	0.036
TruncC	216	0.034397	3.0	0.036	1537	0.028109	3.0	0.026
TruncD	215	0.032251	3.0	0.036	1313	0.025726	3.0	0.026
z=1								
ΛCDM	194	0.032190	2.43	0.036	1745	0.032580	2.96	0.036
TruncB	195	0.028307	3.0	0.031	1760	0.031928	3.0	0.031
TruncC	194	0.029211	2.16	0.036	1673	0.027362	3.0	0.026
TruncD	195	0.028307	3.0	0.031	1435	0.023866	2.89	0.026
z=2								
ΛCDM	115	0.027968	2.47	0.031	1465	0.030142	2.6	0.031
TruncB	116	0.025232	2.81	0.026	1500	0.029746	2.7	0.031
TruncC	116	0.026068	2.72	0.031	1484	0.024087	2.92	0.026
TruncD	116	0.025232	2.81	0.026	439	0.024209	2.78	0.026
z=3								
ΛCDM	58	0.030580	1.86	0.031	987	0.029453	2.67	0.031
TruncB	58	0.030509	2.44	0.031	1016	0.028299	2.3	0.031
TruncC	60	0.032194	1.58	0.036	1032	0.022661	2.42	0.026
TruncD	64	0.032106	2.56	0.031	827	0.019260	3.0	0.021

Table 3. Halo Specific Angular Momentum & Spin : Variation with Redshift $N_{0.2}$ and $N_{0.8}$ give the number of haloes in the "quiescent" (lower 20% of $f(\delta_{\rm max})$) and "violent" (upper 20% of $f(\delta_{\rm max})$) halo samples respectively; β and γ give normalisations and logarithmic slopes of linear regressions to the data; σ indicates the r.m.s. variation; and r_s gives the Spearman rank coefficient.

Run	$N_{\delta_{\rm max}<0.2}$	$N_{\delta_{\rm max}>0.8}$	$\beta_{0.2}$	$\gamma_{0.2}$	$\sigma_{0.2}$	$r_{\rm s,0.2}$	$\beta_{0.8}$	$\gamma_{0.8}$	$\sigma_{0.8}$	$r_{\rm s,0.8}$
$\mathbf{j}=\mathbf{J}/\mathbf{M}$										
ΛCDM	29	51	1.08	1.05	0.29	0.58	1.15	1.66	0.51	0.51
TruncA	41	71	1.24	1.1	0.29	0.59	1.19	2.12	0.49	0.62
TruncB	35	43	1.12	1.14	0.38	0.52	1.33	1.92	0.48	0.58
TruncC	32	36	1.03	0.84	0.30	0.52	1.39	1.85	0.49	0.56
TruncD	46	20	1.17	1.01	0.29	0.53	1.30	2.12	0.52	0.60
λ										
LCDM	29	51	0.05	0.19	0.27	0.14	0.11	0.07	0.39	0.03
TruncA	41	71	0.05	-0.04	0.25	-0.02	0.15	0.11	0.41	0.04
TruncB	35	43	0.06	0.006	0.29	-0.001	0.14	0.14	0.39	0.05
TruncC	32	36	0.04	-0.26	0.27	-0.19	0.13	0.14	0.40	0.06
TruncD	46	20	0.04	-0.11	0.26	-0.08	0.16	0.38	0.42	0.18

are believed to become more important drivers of angular momentum evolution during this phase. Therefore, if there are differences between the models, we would expect them to be apparent in the ratio of the 'peak' angular momentum at turnaround to the final angular momentum at z=0.

In the upper panel of Figure 12 we show the distribution of $J(z_{\rm t})/J(z=0)$ versus halo mass, while in the lower panel we show the cumulative distribution $D(<J(z_{\rm t})/J(z=0))$ for all haloes with masses in excess of $5\times10^{10}h^{-1}\mathrm{M}_{\odot}$ at z=0. For clarity we consider only the ΛCDM (filled circles, solid curves), TruncB (filled squares, dashed curves) and TruncD (crosses, dotted-dashed curves) runs. The upper panel reveals that, on average, the ratio of $J(z_{\rm t})/J(z=0)$ does not vary appreciably with mass and that it is slightly less than unity (approximately 0.8). In other words, the magnitude of the total angular momentum of the material at turnaround is on average smaller than at z=0.

These Figures reveal that there are small differences that we observe in the spin distributions are also present in the specific angular. The median $J(z_{\rm t})/J(z=0)$ differs by $\sim 10\%$ between

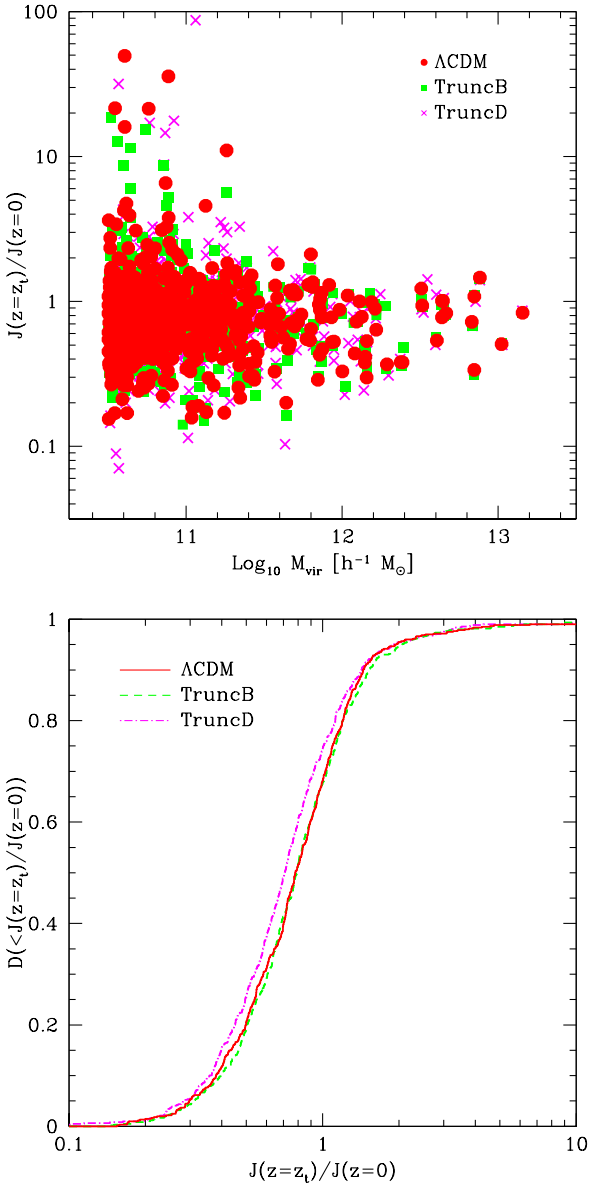

Figure 12. Angular Momentum at Turnaround. We track the material associated with each halo identified at z=0 and compute the radial extent and angular momentum of this material as a function of redshift in the ΛCDM , TruncB and TruncD runs. When the material has reached its maximum radial extent, we denote the epoch at which this occurs as turnaround and look at the ratio of the magnitude of angular momentum of the material at this redshift $z_{\rm t}$, $J(z_{\rm t})$, with respect to the magnitude of the angular momentum of this material at z=0. In the upper panel we show the variation of this ratio with halo mass at z=0; in the lower panel, we show the cumulative distribution $D(< J(z_{\rm t})/J(z=0))$.

the ΛCDM model and the TruncD run.

Specific Angular Momentum Profiles: There does not appear to be any systematic difference in the bulk angular momenta of haloes, i.e. the total angular momentum of material within $r_{\rm vir}$. What of the distribution of angular momentum within $r_{\rm vir}$? We focus on the specific angular momentum profile, which quantifies the fraction of material within the virial radius that has specific angular momentum of j or less. Figure 13 shows the average specific angular momentum profile $M(< j)$ of haloes in each of our models.

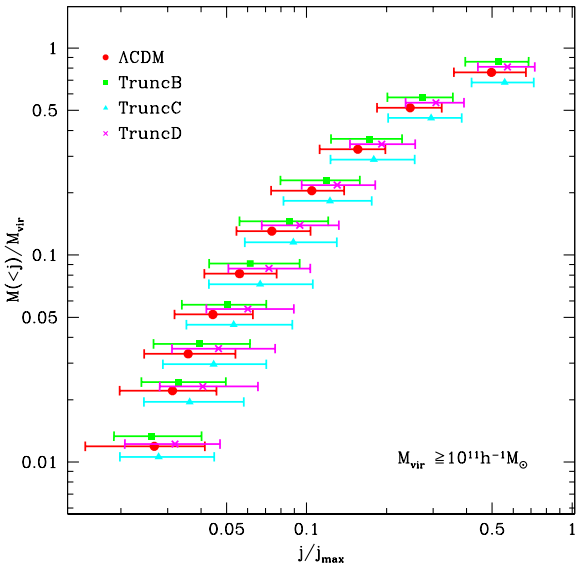

Figure 13. Specific Angular Momentum Profiles. We use the method of Bullock et al. (2001, 2002) to determine the fraction of halo mass that has a total specific angular momentum of j or less. Note that we consider only haloes that satisfy $M_{\rm vir} \geqslant 10^{11}h^{-1}M_{\odot}$.

We compute specific angular momentum profiles using the method presented in Bullock et al. (2001, 2002). In brief, we compute the total angular momentum of the halo and define this as the z-axis; then we sort particles into spherical shells of equal mass and increasing radius, and we assign shell particles to one of three equal volume segments determined by the particle's angle with respect to the z-axis; finally, we compute both the total and z-component of the specific angular momentum in each segment. This allows us to compute the fraction of halo with specific angular momentum of j (and its z component $j_{\rm z}$) or less. Note that we scale our profiles by $j_{\rm max}$, the maximum specific angular momentum that we measure in our data; this is distinct from the $j_{\rm max}$ used in Bullock et al. (2001, 2002), who estimate $j_{\rm max}$ by fitting their universal angular momentum profile.

In Figure 13 we show the specific angular momentum profile for the total angular momentum j, although the j_z behaviour is similar. For ease of comparison, we have applied small offsets to the data points from the truncated-$P(k)$ runs. There are a few points worthy of note in this Figure. The profile gently curves towards shallower logarithmic slopes with increasing j; we find that $M(< j) \sim j^{5/2}$ for the lowest angular momentum material and $M(< j) \sim j^{1/2}$ for the highest angular momentum material. It is interesting that there is a systematic trend for lower angular momentum material in the ΛCDM and TruncB runs to have *on average* lower values of j than the TruncC and TruncD runs – the difference is of order 25% at most. This trend is not evident when one looks at the projected specific angular momentum (j_z) profile. However, the r.m.s. scatter is large for a given $M(< j)$ or $M(< j_{\rm z})$ in all our models, and for interesting values of $M_{\rm cut} \sim 10^9 h^{-1} M_{\odot}$ (comparable to our TruncA run) there is no statistically significant difference.

6 SUMMARY & DISCUSSION

The focus of this paper has been to determine to what extent suppressing the formation of small-scale structure – low-mass dark matter haloes – affects the angular momentum content of galaxy- and group-mass dark matter haloes. Previous studies have suggested that mergers could be important for the growth of halo angular momentum at late (non-linear) times (cf. White 1984; Bailin & Steinmetz 2005) and that minor mergers play a particularly important role (e.g. Vitvitska et al. 2002; Hetznecker & Burkert 2006), although recent work asserts that mergers are unimportant (cf. Wang & White 2008). Nevertheless it is interesting to revisit this topic in detail because of its interesting observable consequences. For example, if the specific angular momentum of a galactic disc is determined by it host halo's angular momentum (cf. Fall & Efstathiou 1980; Mo et al. 1998; Zavala et al. 2008), then observations of the sizes of galactic discs could in principle be used to place limits on the abundance of small-scale structure and consequently the nature of the dark matter.

Using cosmological N-body simulations, we investigated this problem by studying the abundance, clustering and mass assembly histories of dark matter haloes in a fiducial ΛCDM model and in truncated-$P(k)$ models. We explored truncated-$P(k)$ models in which $M_{\rm cut}$ varies between $5\times10^{9}h^{-1}{\rm M}_{\odot}$ and $10^{11}h^{-1}{\rm M}_{\odot}$. We then focussed the angular momentum content of haloes with masses between $M\sim10^{11}$ to $10^{13}h^{-1}M_{\odot}$ (i.e. galaxy- and group-masses) over the redshift range $0\leqslant z\lesssim3$. By taking this approach, we verified that both the abundance of low-mass haloes and their merger rate with galaxy- and group-mass haloes is suppressed in the truncated-$P(k)$ models. The key question then became how the angular momentum content is affected by the absence of small-scale structure. The main results of our study can be summarised as follows;

Large Scale Structure: Visual inspection of the density distribution reveals that the structure that forms in truncated-$P(k)$ models is indistinguishable from that in the ΛCDM model on large scales but differs on small scales. Precisely how small this scale is depends on $M_{\rm cut}$, the mass scale below which low-mass halo formation is suppressed. For $M_{\rm cut}=5\times10^{9}h^{-1}{\rm M}_{\odot}$ the differences with the ΛCDM model are negligible, but they become significant for $M_{\rm cut}=10^{11}h^{-1}{\rm M}_{\odot}$. The degree of significance can be quantified by the halo mass and 2-point correlation functions.

Mass Functions: Compared to the fiducial ΛCDM model, halo mass functions measured in the truncated-$P(k)$ models agree to better than 10% at masses $M_{\rm vir}\gtrsim0.5\,M_{\rm cut}$, whereas there are systematic deviations for $M_{\rm vir}\lesssim0.5\,M_{\rm cut}$. For example, the number density of haloes with $M_{\rm vir}\simeq0.1\,M_{\rm cut}$ is typically $\sim20\%$ lower than in the fiducial ΛCDM run. Interestingly mass functions in the truncated-$P(k)$ models show a characteristic upturn of the kind reported by Wang & White (2007), associated with unphysical haloes that form in N-body simulations in which small-scale power is suppressed at early times. However, the limiting masses that we estimated are smaller than we obtain from the criterion proposed by Wang & White (2007) – by between a factor of ~8 for $M_{\rm cut}=10^{10}h^{-1}M_{\odot}$ and a factor of ~4 for $M_{\rm cut}=10^{11}h^{-1}M_{\odot}$.

Spatial Clustering: The trends observed in the halo mass functions are mirrored in the clustering strength of lower-mass secondary haloes around more massive primary haloes. Assuming that the primary mass is fixed at $M_{\rm vir}=10^{11}h^{-1}{\rm M}_{\odot}$, we found that the clustering strength of secondaries around primaries depends strongly on $M_{\rm cut}$ and the minimum secondary mass. If we include secondaries with masses $M_{\rm vir}\geqslant3\times10^{9}h^{-1}{\rm M}_{\odot}$, the differences are as great as $\sim50\%$ when $M_{\rm cut}$=$10^{11}h^{-1}\,{\rm M}_{\odot}$. Unsurprisingly, we found no dependence on $M_{\rm cut}$ if secondaries are restricted to haloes with masses $M_{\rm vir}\geqslant10^{11}h^{-1}{\rm M}_{\odot}$.

Mass Accretion and Merger Rates: We found that the sensitivity to $M_{\rm cut}$ of the clustering strength of low-mass haloes around more massive haloes has immediate consequences for the frequency of minor mergers. The effect is most striking for models with $M_{\rm cut}\geqslant5\times10^{10}h^{-1}\,{\rm M}_{\odot}$, when the rate of all mergers with mass ratios in excess of $\sim6\%$ is suppressed across all redshifts by factors of ~2 to 3 in haloes with virial masses of $M_{\rm vir}\lesssim5\times10^{11}h^{-1}{\rm M}_{\odot}$. This effect must be driven by a reduction in the number of minor mergers because the frequency of major mergers does not depend on $M_{\rm cut}$ other than in haloes with masses $M_{\rm vir}\sim M_{\rm cut}$. Interestingly we found that the total mass accretion rate does not appear to be sensitive to $M_{\rm cut}$ at all.

Halo Angular Momentum: Despite the measurable differences in the rate of minor mergers, we found no evidence to suggest that the angular momentum content of galaxy- and group-mass haloes are sensitive to $M_{\rm cut}$. First, we computed the spin parameter λ for all haloes with $M_{\rm vir}\geqslant2\times10^{10}h^{-1}{\rm M}_{\odot}$ between $0\leqslant z\lesssim3$. We found that the median spin of haloes with $M_{\rm vir}\geqslant10^{11}h^{-1}{\rm M}_{\odot}$ measured in different models shows no obvious dependence on $M_{\rm cut}$. Rather the quiescence or violence of a halo's mass accretion history has – on average – a greater bearing on its spin parameter. We found a marked systematic offset between the average spins of haloes with violent mass accretion histories and those with quiescent histories – by a factor of ~2 to 3, independent of $M_{\rm cut}$. Interestingly we also found that the spin of individual halo evolves in an almost stochastic fashion over time and on average it does not show any obvious evolution with redshift.

Second, we focused on the distribution of angular momentum within individual haloes by computing the specific angular momentum profiles. This provides quantifies the fraction of material within a halo that has specific angular momentum of j or less. There is a suggestion of a weak trend for halo material in the ΛCDM model and truncated-$P(k)$ model with $M_{\rm cut}$=$10^{10}h^{-1}\,{\rm M}_{\odot}$ to have on average smaller values of j by 25% at most, but the r.m.s scatter is large for a given $M(<j)$ in all our models and the differences have a low statistical significance.

Third, we investigated the angular momentum of the Lagrangian region corresponding to the virialised halo at z=0 and determined how it evolves with time. We calculated $J(z_{\rm t})/J(z=0)$, the ratio of the angular momentum of the material at the turnaround redshift $z_{\rm t}$ to z=0. The differences between the models are small, at most 10%.

These results demonstrate that small-scale structure has little impact on the angular momentum content of galaxy- and group-mass haloes. Indeed, any differences between the angular momenta of haloes in CDM and truncated-$P(k)$ models become apparent when one looks at the distribution of the spin parameter λ and includes haloes with masses below $M_{\rm cut}$. In these cases one finds systematically smaller median values of λ as $M_{\rm cut}$ increases, but this reflects differences in halo concentrations rather than halo angular momentum. Smaller concentrations imply smaller values of energy $|E|$ which in turn implies smaller values of λ; because the number of low-mass haloes continues to increase with decreasing mass be-

low $M_{\rm cut}$ (albeit at a slower rate) the haloes with $M \lesssim M_{\rm cut}$ will have greater leverage over the median of the distribution than those with $M \gtrsim M_{\rm cut}$.

Our results agree with those of Wang & White (2008). They studied general halo properties in a Hot Dark Matter (HDM) model with a damping mass of $\sim 7.5\times10^{14}h^{-1}{\rm M}_{\odot}$. Even in this extreme case, they found that the distribution of spins and internal angular momentum in their HDM model and a fiducial CDM model were in excellent agreement, and concluded that merging is unimportant. A similar conclusion was reached by both Bullock et al. (2002) and Chen & Jing (2002), who looked at the internal angular momentum distribution of haloes in WDM models.

What does this mean? On the one hand we do not expect the tidal field that is responsible for tidally torquing proto-haloes to differ between the truncated-$P(k)$ and ΛCDM runs. Rather it is $M_{\rm cut}$ that varies, which affects a halo's merging history. In the TruncC and TruncD models the effect of $M_{\rm cut}$ is most dramatic (affecting the frequency of not only minor but also major mergers), yet we find no evidence for systematic differences in halo angular momenta for haloes with masses $M \gtrsim M_{\rm cut}$ between different models. In other words, a halo's minor merger history is unimportant for setting halo angular momentum.

This does not necessarily argue against merger history playing a role in setting λ, but it does suggest that major rather than minor mergers are key. We have followed the redshift evolution of individual haloes' specific angular momenta and spins, separating the haloes into those with quiescent ($\delta_{\rm max} \leqslant 0.2$) and violent ($\delta_{\rm max} \geqslant 0.2$) merging histories. The spin parameter is a noisy quantity but on average its value depends at best weakly on time. Interestingly those haloes with quiescent merging histories have on average smaller values of λ than haloes with violent merging histories. What is particularly interesting is that haloes with violent merging histories have systematically larger values of the spin parameter and they show dramatic jumps in spin, which correlates with recent merging, but on average their spins are also reasonably constant with time. This hints at an environmental dependence because violent merging history correlates with how overdense and environment the halo resides in. This would seem to support the assertion of D'Onghia & Navarro (2007) who have argued that it is the redistribution of matter that drives the growth of halo spin.

How then can we differentiate between a CDM model in which low-mass haloes are present but dark and one in which low-mass halo formation is suppressed? Our results suggest that there are differences in the abundance and spatial clustering of low-mass haloes around their more massive counterparts in dark matter models in which small-scale power has been suppressed at early times, and that this has a bearing on the minor merger rate for haloes with masses close to the cut-off mass $M_{\rm cut}$. In contrast, there is no discernible effect on the angular momentum content of these haloes. Measuring the effect on spatial clustering or the merger rate is likely to be observationally difficult for realistic values of $M_{\rm cut}$, equivalent to our TruncA runs, and so isolating the effect of this small-scale structure would appear to be remarkably difficult, at least in the present day Universe. In this case, measurements of cosmic shear (e.g. Markovic et al. 2011) and the Lyman-α forest (cf. Viel et al. 2011), and the presence of dark matter cusps in Local Group dwarf satellies – inferred from γ-ray fluxes via dark matter annihilation (cf. Charbonnier et al. 2011) and precise measurements of their stellar kinematics (e.g. Gilmore et al. 2008) – are likely to provide more robust tests of the CDM model.

Differences between the halo populations in the fiducial CDM model and WDM(-like) models will be most pronounced at early times, and so we might expect to find the imprint in the earliest generations of galaxies. For example, Gao & Theuns (2007) have shown that the properties of the first generation stars in a class of WDM models can be quite different from those predicted in the CDM model. These authors adopted a WDM particle mass of $3{\rm keV}$ (corresponding to a cut-off mass of $M_{\rm cut} \sim 3\times10^{8}M_{\odot}$). CDM models predict that the initial mass function of the first stars is top-heavy; that is, the formation of high to extremely high mass stars is favoured. In contrast, Gao & Theuns (2007) showed that low- to intermediate-mass stars form in their adopted WDM model, and they argued that such stars could help explain present day observations of extremely metal poor stars of the kind detected in the Hamburg/ESO survey (e.g. Christlieb et al. 2002; Frebel 2005).

Here it becomes particularly interesting to examine differences between models, incorporating prescriptions (either by means of hydrodynamical simulations or semi-analytical modelling) that can provide insights into gas transport in the presence or absence of dark matter small-scale (or sub) structure. What kind of global stellar IMF can we expect, and what are the implications for the seed masses of super-massive black holes? How efficiently can super-massive black holes grow, or bulges form? These differences in the cold gas rather than stellar structure of galaxies could in principle be accessible by surveys on next generation radio telescopes such as ALMA (e.g. Solomon & Vanden Bout 2005) and the SKA (e.g. van der Hulst et al. 2004), while differences in the ionising radiation field at early times could be probed by arrays such as the MWA, LOFAR and the SKA (e.g. Zaroubi 2010). We shall return to these issues, both theoretical and observational, in forthcoming work.

ACKNOWLEDGMENTS

CP acknowledges the support of the STFC theoretical astrophysics rolling grant at the University of Leicester. GL acknowledges funding through the Australian Research Council funded "Commonwealth Cosmology Initiative", DP Grant No. 0665574. JBH is funded by a Federation Fellowship from the Australian Research Council. This research used the ALICE High Performance Computing Facility at the University of Leicester. Some resources on ALICE form part of the DiRAC Facility jointly funded by STFC and the Large Facilities Capital Fund of BIS.

REFERENCES

Avila-Reese V., Colín P., Valenzuela O., D'Onghia E., Firmani C., 2001, ApJ, 559, 516
Bagla J. S., Ray S., 2005, MNRAS, 358, 1076
Bailin J., Steinmetz M., 2005, ApJ, 627, 647
Bardeen J. M., Bond J. R., Kaiser N., Szalay A. S., 1986, ApJ, 304, 15
Benson A. J., Lacey C. G., Baugh C. M., Cole S., Frenk C. S., 2002, MNRAS, 333, 156
Bergström L., 2000, Reports of Progress in Physics, 63, 793
Bett P., Eke V., Frenk C. S., Jenkins A., Helly J., Navarro J., 2007, MNRAS, 376, 215
Bode P., Ostriker J. P., Turok N., 2001, ApJ, 556, 93
Boehm C., Mathis H., Devriendt J., Silk J., 2005, MNRAS, 360, 282

Bullock J. S., Kolatt T. S., Sigad Y., Somerville R. S., Kravtsov A. V., Klypin A. A., Primack J. R., Dekel A., 2001, MNRAS, 321, 559
Bullock J. S., Kravtsov a. A. V., Colín P., 2002, ApJ, 564, L1
Charbonnier A., Combet C., Daniel M., Funk S., Hinton J. A., Maurin D., Power C., Read J. I., Sarkar S., Walker M. G., Wilkinson M. I., 2011, ArXiv e-prints
Chen D. N., Jing Y. P., 2002, MNRAS, 336, 55
Chen J., Kravtsov A. V., Keeton C. R., 2003, ApJ, 592, 24
Christlieb N., Bessell M. S., Beers T. C., Gustafsson B., Korn A., Barklem P. S., Carlsson T., Mizuno-Wiedner M., Rossi S., 2002, Nature, 419, 904
Cole S., Lacey C., 1996, MNRAS, 281, 716
Colín P., Avila-Reese V., Valenzuela O., 2000, ApJ, 542, 622
Colín P., Valenzuela O., Avila-Reese V., 2008, ApJ, 673, 203
Dalal N., Kochanek C. S., 2002, ApJ, 572, 25
de Vega H. J., Sanchez N. G., 2011, ArXiv e-prints
Dekel A., Silk J., 1986, ApJ, 303, 39
Diemand J., Kuhlen M., Madau P., 2007, ApJ, 657, 262
D'Onghia E., Navarro J. F., 2007, MNRAS, 380, L58
Dunstan R. M., Abazajian K. N., Polisensky E., Ricotti M., 2011, ArXiv e-prints
Efstathiou G., 1992, MNRAS, 256, 43P
Eke V. R., Cole S., Frenk C. S., 1996, MNRAS, 282, 263
Evans N. W., Witt H. J., 2003, MNRAS, 345, 1351
Fall S. M., Efstathiou G., 1980, MNRAS, 193, 189
Font A. S., Navarro J. F., Stadel J., Quinn T., 2001, ApJ, 563, L1
Frebel A., 2005, Nature, 434, 871
Gao L., Theuns T., 2007, Science, 317, 1527
Gao L., White S. D. M., 2006, MNRAS, 373, 65
Gao L., White S. D. M., Jenkins A., Stoehr F., Springel V., 2004, MNRAS, 355, 819
Gilmore G., Zucker D., Wilkinson M., Wyse R. F. G., Belokurov V., Kleyna J., Koch A., Evans N. W., Grebel E. K., 2008, in T. Kodama, T. Yamada, & K. Aoki ed., Panoramic Views of Galaxy Formation and Evolution Vol. 399 of Astronomical Society of the Pacific Conference Series, What Is a Galaxy? How Cold Is Cold Dark Matter? Recent Progress in Near Field Cosmology. pp 453–+
Green A. M., Hofmann S., Schwarz D. J., 2004, MNRAS, 353, L23
Hetznecker H., Burkert A., 2006, MNRAS, 370, 1905
Kazantzidis S., Bullock J. S., Zentner A. R., Kravtsov A. V., Moustakas L. A., 2008, ApJ, 688, 254
Klypin A., Kravtsov A. V., Valenzuela O., Prada F., 1999, ApJ, 522, 82
Knebe A., Devriendt J. E. G., Mahmood A., Silk J., 2002, MNRAS, 329, 813
Knollmann S. R., Knebe A., 2009, ArXiv e-prints
Lewis G. F., Bland-Hawthorn J., Gibson B. K., Putman M. E., 2000, PASP, 112, 1300
Łokas E. L., Mamon G. A., 2001, MNRAS, 321, 155
Lukić Z., Heitmann K., Habib S., Bashinsky S., Ricker P. M., 2007, ApJ, 671, 1160
Maller A. H., Dekel A., Somerville R., 2002, MNRAS, 329, 423
Mao S., Schneider P., 1998, MNRAS, 295, 587
Markovic K., Bridle S., Slosar A., Weller J., 2011, Journal of Cosmology and Astroparticle Physics, 1, 22
Maulbetsch C., Avila-Reese V., Colín P., Gottlöber S., Khalatyan A., Steinmetz M., 2007, ApJ, 654, 53
Mo H. J., Mao S., White S. D. M., 1998, MNRAS, 295, 319
Moore B., 1994, Nature, 370, 629
Moore B., Ghigna S., Governato F., Lake G., Quinn T., Stadel J., Tozzi P., 1999, ApJ, 524, L19
Moore B., Quinn T., Governato F., Stadel J., Lake G., 1999, MNRAS, 310, 1147
Natarajan P., De Lucia G., Springel V., 2007, MNRAS, 376, 180
Natarajan P., Springel V., 2004, ApJ, 617, L13
Peebles P. J. E., 1969, ApJ, 155, 393
Power C., Knebe A., 2006, MNRAS, 370, 691
Power C., Knebe A., Knollmann S. R., 2011, ArXiv e-prints
Prada F., Klypin A. A., Simonneau E., Betancort-Rijo J., Patiri S., Gottlöber S., Sanchez-Conde M. A., 2006, ApJ, 645, 1001
Primack J. R., 2009, ArXiv e-prints
Reed D. S., Bower R., Frenk C. S., Jenkins A., Theuns T., 2007, MNRAS, 374, 2
Seljak U., Zaldarriaga M., 1996, ApJ, 469, 437
Shaw L. D., Weller J., Ostriker J. P., Bode P., 2006, ApJ, 646, 815
Sheth R. K., Tormen G., 1999, MNRAS, 308, 119
Sheth R. K., Tormen G., 2002, MNRAS, 329, 61
Smith R. E., Markovic K., 2011, Phys. Rev. D, 84, 063507
Solomon P. M., Vanden Bout P. A., 2005, ARA&A, 43, 677
Spergel D. N., 2007, ApJS, 170, 377
Springel V., 2005, MNRAS, 364, 1105
Sugerman B., Summers F. J., Kamionkowski M., 2000, MNRAS, 311, 762
Thoul A. A., Weinberg D. H., 1996, ApJ, 465, 608
Tremaine S., Gunn J. E., 1979, Physical Review Letters, 42, 407
van der Hulst J. M., Sadler E. M., Jackson C. A., Hunt L. K., Verheijen M., van Gorkom J. H., 2004, New Astronomy, 48, 1221
Viel M., Markovic K., Baldi M., Weller J., 2011, ArXiv e-prints
Vitvitska M., Klypin A. A., Kravtsov A. V., Wechsler R. H., Primack J. R., Bullock J. S., 2002, ApJ, 581, 799
Wang J., White S. D. M., 2007, MNRAS, 380, 93
Wang J., White S. D. M., 2008, ArXiv e-prints
White S. D. M., 1984, ApJ, 286, 38
White S. D. M., 1994, ArXiv Astrophysics e-prints
White S. D. M., Frenk C. S., 1991, ApJ, 379, 52
White S. D. M., Rees M. J., 1978, MNRAS, 183, 341
Xu D. D., Mao S., Wang J., Springel V., Gao L., White S. D. M., Frenk C. S., Jenkins A., Li G., Navarro J. F., 2009, MNRAS, 398, 1235
Zaroubi S., 2010, ArXiv e-prints
Zavala J., Okamoto T., Frenk C. S., 2008, MNRAS, 387, 364